

Dusk-Dawn Asymmetries in SuperDARN Convection Maps

M.-T. Walach¹, A. Grocott¹, E. G. Thomas², F. Staples³

¹Lancaster University, Lancaster, LA1 4YW, UK

²Thayer School of Engineering, Dartmouth College, Hanover, NH, USA

³Department of Atmospheric and Oceanic Sciences, University of California, Los Angeles, CA, USA

Key Points:

- We study dusk-dawn asymmetries in 7 years of SuperDARN convection maps which are introduced by different solar wind orientations, or the data processing
- Asymmetries due to IMF B_y can occur in the strength and location of the convection cells, and the return flow width
- Asymmetries due to the background model are likely to occur in the locations of the convection cells

Corresponding author: Maria-Theresia Walach, m.walach@lancaster.ac.uk

Abstract

The Super Dual Auroral Radar Network (SuperDARN) is a collection of radars built to study ionospheric convection. We use a 7-year archive of SuperDARN convection maps, processed in 3 different ways, to build a statistical understanding of dusk-dawn asymmetries in the convection patterns. We find that the dataset processing alone can introduce a bias which manifests itself in dusk-dawn asymmetries. We find that the solar wind clock angle affects the balance in the strength of the convection cells. We further find that the location of the positive potential foci is most likely observed at latitudes of 78° for long periods (>300 minutes) of southward IMF, as opposed to 74° for short periods (<20 minutes) of steady IMF. For long steady dawnward IMF the median is also at 78° . For long steady periods of duskward IMF, the positive potential foci tends to be at lower latitudes than the negative potential and vice versa during dawnward IMF. For long periods of steady Northward IMF, the positive and negative cells can swap sides in the convection pattern. We find that they move from $\sim 0-9$ MLT to 15 MLT or $\sim 15-23$ MLT to 10 MLT, which reduces asymmetry in the average convection cell locations for Northward IMF. We also investigate the width of the region in which the convection returns to the dayside, the return flow width. Asymmetries in this are not obvious, until we select by solar wind conditions, when the return flow region is widest for the negative convection cell during Southward IMF.

Plain Language Summary

At high latitudes, near the Earth's magnetic pole, the ionosphere moves around in a dual-cell pattern: The convection moves from the dayside, over the magnetic pole towards the nightside and then flows return back to the dayside at lower latitudes. Both cells tend to be centred away from the pole, one towards the dusk side and one towards the dawn side. The two cells have a tendency to be asymmetric with the dusk cell typically larger and stronger. Asymmetries in the two convection cells are often attributed to changes in the solar wind as there is a physical connection between the ionosphere and the solar wind. The mechanisms which describe this interaction are well known but some of the datasets with which we measure ionospheric convection have unquantified uncertainties associated with them. One of the longest running measurement systems of the ionospheric convection is the Super Dual Auroral Radar Network (SuperDARN). This ground-based system was built specifically to measure ionospheric convection and it is often used to make convection maps of the ionosphere. Over the years, more radars have been added to the network and the software used to process the data has been updated. In this study we use different versions of the convection maps to statistically investigate 6 years of ionospheric convection asymmetries and understand which of the asymmetries were introduced by a change in the dataset and which by the solar wind. We look at the location and strength of the cells and the width of the return flow region, which constrains the size of the cells.

1 Introduction**1.1 Ionospheric Convection**

Ionospheric convection results from the flow of magnetic flux in the magnetosphere. The convection informs on the state of the magnetosphere and accurate measurements of convective electric fields in the ionosphere are important to correctly interpret global magnetospheric dynamics. A common way to remote sense the convection on a global scale, is to use convection maps. Convection maps are large scale maps, showing ionospheric convection around the magnetic poles. Ionospheric convection maps usually show a two-cell convection pattern with the ionospheric plasma flowing from the dayside across the polar region towards the nightside (e.g. Greenwald et al., 1995). From there, the ionospheric plasma moves back to the dayside at lower latitudes. This convection pattern

64 is understood to change according to the solar wind driving of the magnetosphere-ionosphere
 65 system and nightside responses (e.g. S. W. Cowley, 1981a; S. Cowley, 1981b; S. W. H. Cow-
 66 ley, 1982; S. W. H. Cowley et al., 1991; M. Freeman et al., 1991; S. W. H. Cowley & Lock-
 67 wood, 1992, 1996; S. W. H. Cowley, 2000; Grocott et al., 2002, 2003; M. P. Freeman, 2003;
 68 Lockwood & Morley, 2004; Grocott et al., 2008; Milan et al., 2017; Walach et al., 2017).

69 Solar wind coupling of the magnetosphere-ionosphere system not only drives activ-
 70 ity but also asymmetries. A non-zero IMF B_y component will impose a torque on the
 71 magnetic field flux tubes and affect their transport from the dayside to the nightside (S. W. Cow-
 72 ley, 1981a). This imposes a twist in the open magnetic flux and results in a skewed iono-
 73 spheric convection pattern (e.g. Ruohoniemi & Greenwald, 2005; Haaland et al., 2007).
 74 For example the dawn convection cell is typically smaller than the dusk cell and a posi-
 75 tive IMF B_y component rotates the convection cell patterns, such that the main flow
 76 channel goes across the polar cap, from 10:00 to 21:00 MLT (e.g. Walsh et al., 2014).

77 Even without an IMF B_y component however, the convection cells are rarely sym-
 78 metric about the noon-midnight meridian. Whilst much of the ionospheric convection
 79 dynamics are attributed to solar wind driving of the magnetosphere, this lack of sym-
 80 metry about the noon-midnight meridian can be attributed to nonuniformities in iono-
 81 spheric conductivity (Atkinson & Hutchison, 1978). The strong conductivity gradients
 82 in the ionosphere across the day-night terminator squeezes the plasma flow more strongly
 83 toward the dawnside of the polar cap, which can be modelled by simulations (Tanaka,
 84 2001). The result is a slight clockwise rotation to the convection pattern, which then re-
 85 sults in the open flux being diverted towards the duskside of the magnetotail. The re-
 86 connection in the plasma sheet is thus also asymmetric and further introduces asymme-
 87 tries into the magnetosphere (Smith, 2012). A prevailing IMF B_y component can intro-
 88 duce asymmetries which not only dictate substorm onset location but also enhance the
 89 asymmetries further (Grocott et al., 2017). Another resulting plasma flow due to asym-
 90 metries is the Sub-Auroral Polarization Stream (SAPS), which are separate and equa-
 91 torward of the convection pattern (e.g. Yeh et al., 1991; Foster & Vo, 2002). Whilst SAPS
 92 coincide with fast flows in the ionosphere, they are said to be a separate phenomenon
 93 from convection but questions around their generation mechanism remain: For exam-
 94 ple, Sangha et al. (2020) observed SAPS as a direct result of a bifurcation in the Region-
 95 2 currents, which means they may be, at least initially, directly connected to the con-
 96 vection cells and thus contribute to asymmetries in the convection pattern or arise from
 97 such.

98 1.2 SuperDARN Convection Maps

99 Convection maps provide a useful tool in studying ionospheric convection. A well-
 100 established way to construct these is to combine data from the Super Dual Auroral Radar
 101 Network (SuperDARN). This consists of high-frequency coherent scatter radars built to
 102 study ionospheric convection by means of Doppler-shifted pulse sequences and has been
 103 widely used in space physics and ionospheric research (e.g. Greenwald et al., 1995; Ruo-
 104 honiemi & Greenwald, 1996; Chisham et al., 2007; Nishitani et al., 2019). SuperDARN
 105 data are continuously available from 1993, with the network having expanded over time
 106 from one radar (built in 1983) to 23 radars in the Northern hemisphere, 13 in the South-
 107 ern hemisphere and more under construction. This expansion has allowed for a greater
 108 area to be covered by SuperDARN (i.e. down to magnetic latitudes of 40°) with at least
 109 16 different look directions for each radar along which different ranges can be sampled.
 110 Line-of-sight measurements by this large-scale network of radars can be combined and
 111 used to construct a picture of high-latitude ionospheric convection on time scales of 1-
 112 2 minutes (Ruohoniemi & Baker, 1998). The radars can be grouped into high-latitude
 113 radars (the original network), polar-latitude radars (or PolarDARN), and mid-latitude
 114 radars (or StormDARN). Nishitani et al. (2019) provides a summary from a historical
 115 northern hemisphere perspective: high-latitude radars, at magnetic latitudes of $50-70^\circ$

116 were first built, starting in 1983 with the Goose Bay radar, followed by the PolarDARN
 117 radars (covering 70-90° magnetic latitude), and the expansion to mid-latitudes ($\sim 40\text{-}50^\circ$),
 118 starting in 2005 with the Wallops Island radar. Over time new radars have added to the
 119 global ionospheric convection mapping increasing the number of measurements and look
 120 directions. The SuperDARN data product most commonly used by the space science and
 121 ionospheric research community is the convection map.

122 In order to produce SuperDARN convection maps, five key data processing steps
 123 have to be undertaken: (1) Data from different radars are median filtered and combined
 124 onto an equal area polar grid. This allows for (2) the exclusion of data from particular
 125 radars or the specification of a range limit for the scatter. For example, slow moving E-
 126 region scatter can and should be removed by setting the minimum range gate limit to
 127 800 km (an empirical suggestion from Forsythe and Makarevich (2017); Thomas and Shep-
 128 herd (2018)). It has become apparent that far range data beyond 2000 km may also be
 129 problematic owing to geolocation uncertainties in the range finding algorithm (Chisham
 130 et al., 2008; Thomas & Shepherd, 2022). (3) Once the data have been filtered and com-
 131 bined, the latitude of the equatorward extent of the convection, or equivalently the lat-
 132 itude of zero electrostatic potential, is determined. This is done by fitting the data to
 133 a Heppner-Maynard Boundary (HMB) (Heppner & Maynard, 1987; Shepherd & Ruoh-
 134 oniemmi, 2000). (4) Data from an empirical statistical model, hereafter referred to as the
 135 ‘background model’, is then added to the grid. The model is parameterised by a mix of
 136 IMF conditions and solar wind velocity depending on the model. Inclusion of this data
 137 is necessary to ensure a sufficient spatial distribution of data for the subsequent step. (5)
 138 A fitting algorithm is applied which fits an electrostatic potential in terms of spherical
 139 harmonic functions to the data (Ruohoniemi & Greenwald, 1996; Ruohoniemi & Baker,
 140 1998). To find the optimal solution for the spherical harmonic coefficients, a singular value
 141 decomposition (e.g. Press, W. H. and Teukolsky, S. A. and Vetterling W. T. and Flan-
 142 nery B. P., 2007) is minimised. This method is also known as the ‘Map Potential’ tech-
 143 nique. With the expansion of the radar network, as well as data processing software im-
 144 provements, the resulting data product has undergone several changes.

145 Grocott et al. (2012) studied the dependence of the convection patterns on the IMF
 146 using the spherical harmonic coefficients from the convection maps and found IMF B_Y -
 147 dependencies on the magnitude of the dawn and dusk electric potentials. Grocott and
 148 Milan (2014) studied the time-dependence of the SuperDARN convection cells by com-
 149 puting the mean of the spherical harmonic coefficients for different solar wind clock an-
 150 gles and steadiness timescales of the solar wind. They found that the steadiness of the
 151 solar wind is important for introducing asymmetries into the convection maps: if the IMF
 152 clock angle stays in one sector for longer, asymmetries introduced by the solar wind, such
 153 as the dusk-dawn asymmetry in the size of the convection cell become more pronounced.
 154 For example, if the IMF is pointing downward ($B_Y -$), the dusk cell tends to enhance
 155 and the convection throat rotates towards the afternoon sector, whereas when the IMF
 156 is pointing duskward ($B_Y +$), the convection throat tends to rotate towards the early morn-
 157 ing sector. An interesting finding from Grocott and Milan (2014) is that the dawn cell
 158 is, on average, always smaller than the dusk cell under all IMF conditions.

159 Studies looking at dusk-dawn convection asymmetries using SuperDARN, such as
 160 the one by Grocott and Milan (2014), have often used averaging to draw conclusions,
 161 but questions remain on how persistent some of the asymmetry features are? Further-
 162 more, the SuperDARN data availability and data processing have changed over the years
 163 and it is reasonable to assume that these may further affect measured asymmetries: Walach
 164 et al. (2022) conducted a large scale analysis of how changes to data availability and new
 165 mapping techniques has influenced derived convection maps over the history of Super-
 166 DARN operations. The authors found that the expansion of the radar network and pro-
 167 cessing decisions can have a measurable impact on the resulting convection map dataset.
 168 It was shown that when the number of backscatter points per map is high ($n > 200$),

169 the fitting is more reliable, especially when a range limit is applied. Walach et al. (2022)
 170 also showed that for low n maps, the cross polar cap potential (CPCP) is often relying
 171 on the background model. This is particularly apparent when the RG96 (Ruohoniemi
 172 & Greenwald, 1996) model is used as the model bins are discrete, whereas more mod-
 173 ern models such as TS18 (Thomas & Shepherd, 2018) and Cousins and Shepherd (2010)
 174 are able to interpolate between model bins and therefore avoid obvious model-bias. The
 175 Heppner-Maynard Boundary (HMB) (Heppner & Maynard, 1987), the low-latitude bound-
 176 ary where the convection speeds approach 0 m/s, also suffers from this model-dependent
 177 quantization. This previous study also showed that introducing PolarDARN radars tends
 178 to decrease the cross polar cap potential (CPCP), the total electrostatic potential which
 179 the cells hold. Adding StormDARN radars to the network on the other hand, tends to
 180 increase the CPCP.

181 An aspect that was not covered by Walach et al. (2022) is the effect of the changes
 182 in the SuperDARN convection map dataset on the dusk-dawn asymmetries. Asymme-
 183 tries in the electrostatic potential, as well as the location of the convection cells will af-
 184 fect the map morphologies and can therefore affect scientific conclusions drawn.

185 In this paper we probe the effects on dusk-dawn asymmetries statistically to sys-
 186 tematically isolate the effects of;

- 187 1. Differing IMF conditions for short and long timescales of IMF steadiness,
- 188 2. A limited dataset with High-latitude and PolarDARN data only,
- 189 3. A more complete dataset with the addition of the StormDARN data,
- 190 4. Updating of the background statistical model from RG96 to TS18,

191 and the asymmetries introduced by these.

192 Using the same dataset as in Walach et al. (2022), we study the strength and lo-
 193 cation of the negative and positive potential cells, as well as the size of the return flow
 194 region. This allows us to investigate any large-scale dusk-dawn asymmetries in the con-
 195 vection map dataset.

196 2 Methods

197 2.1 SuperDARN Data Processing

198 To provide a meaningful large scale comparison of different versions of the Super-
 199 DARN dataset, we process Northern hemisphere data to create different versions of the
 200 SuperDARN convection maps for the same time period (2012-2018). To make SuperDARN
 201 convection maps we process the raw data using the Radar Software Toolkit (RST (SuperDARN
 202 Data Analysis Working Group et al., 2018)), which can be broken down into the 5 steps
 203 summarized in section 1.2 and described in detail in Walach et al. (2022). For Walach
 204 et al. (2022), we created 5 versions of the dataset to compare to each other (D0 to D4),
 205 but here we will only use 3 (D1, D3 and D4) as these are found to exhibit the most ap-
 206 parent differences in dusk-dawn asymmetries. For detailed information on the data pro-
 207 cessing, we refer the reader to the appendix in Walach et al. (2022). The D1 dataset in-
 208 cludes the high-latitude radars only with a range limit and the RG96 background model.
 209 The basic data processing is the same for all the datasets, except for the following dif-
 210 ferences (see also Table 1 in Walach et al. (2022)):

- 211 • D1: High-latitude radars only with range limit and RG96
- 212 • D3: High-latitude, PolarDARN and StormDARN radars (all radars) with range
 213 limit and RG96
- 214 • D4: High-latitude, PolarDARN and StormDARN radars (all radars) with range
 215 limit and TS18

216 Convection maps are calculated for each dataset using the varying combination of
 217 map data and background model. Datasets D1 and D3 use the Ruohoniemi and Green-
 218 wald (1996) (RG96) background model, whereas dataset D4 uses the more up to date
 219 Thomas and Shepherd (2018) (TS18) background model. By including PolarDARN and
 220 StormDARN radars in datasets D3 and D4, and using the most up to date background
 221 model in D4, we simulate the historical expansion of the SuperDARN dataset and up-
 222 dates to mapping techniques.

223 Range limits are added to datasets D1-D4 to attempt to reduce all possible E-Region
 224 scatter and backscatter with higher uncertainties in projected location (Chisham et al.,
 225 2008; Forsythe & Makarevich, 2017; Thomas & Shepherd, 2018). When the range lim-
 226 its are applied, only backscatter data between 800-2000 km is included. This is the best
 227 solution on a statistical level, and applying these range limits will remove most E-region
 228 scatter (from ranges less than 800 km) and most of the data with higher uncertainty (from
 229 ranges greater than 2000 km).

230 Comparing D1 against D4 allows us to see how the historical version of the dataset
 231 compares to the most modern set-up. This means we can clearly distinguish the asym-
 232 metries created by a limited dataset with fewer radars, compared to a more complete
 233 dataset with all the radars. Comparing D3 against D4 on the other hand, allows us to
 234 see the direct influence of the background model on the convection maps created with
 235 the same radar data. The RG96 model is the oldest background model available and this
 236 was built when only radar data from the Goose Bay radar was available using data from
 237 1987 to 1993 (Ruohoniemi & Greenwald, 1996), whereas the TS18 background model was
 238 built using all the radar data from 23 radars for 2010 to 2016 (inclusive). The data used
 239 for these two background models differs not only in extent but also due to different so-
 240 lar wind conditions brought by the varying solar cycle. Though the sunspot number was
 241 higher for the data used for the RG96 model, the number of radars creates more differ-
 242 ences in the model than the underlying solar cycle (Thomas & Shepherd, 2018).

243 2.2 Convection Map Parameters

244 Having established this archive of 2-minute resolution convection map files, we ex-
 245 tract a set of measured parameters with which to quantify the dusk-dawn asymmetries
 246 in the ionospheric convection maps. We extract the strength and location of the nega-
 247 tive and positive electrostatic potential cells, as well as their latitudinal distance to the
 248 HMB, which we will from now on refer to as the the return flow width. The strength of
 249 the negative and positive potentials are simply the lowest and highest potentials in the
 250 map, respectively, which is a standard output from the map potential technique. The
 251 return flow width is the latitudinal distance between the cell centre (i.e. the location of
 252 the peak in the negative or positive potential) and the HMB at the same magnetic lo-
 253 cal time (MLT). The return flow region is a key indicator of geomagnetic activity. For
 254 the same potential gradient, a narrow region will mean the voltage is distributed over
 255 a smaller width leading to faster flows in the ionosphere, whereas a larger width for the
 256 same potential gradient will mean slower convective flows. An asymmetry in the return
 257 flow width between dusk and dawn, will mean that one side of the magnetosphere sees
 258 increased plasma convection in comparison to the other. Such an asymmetry will be linked
 259 to asymmetries in magnetospheric morphologies and it is thus important to character-
 260 ize.

261 Figure 1 shows an example of four instantaneous convection maps, which we have
 262 chosen to illustrate the extracted measurements and the solar wind conditions by which
 263 we further sub-sample. We have chosen example maps from time periods when the so-
 264 lar wind has pointed in the same solar wind direction ($\pm 15^\circ$) for more than 300 minutes.
 265 Each map is labelled with the relevant solar wind conditions and these are also shown
 266 by the red vector in the clock-angle diagram to the top right of each convection map.

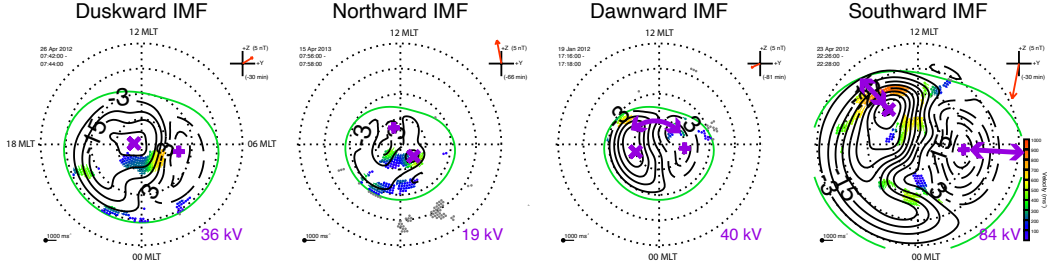


Figure 1. Four instantaneous convection maps showing the four solar wind conditions by which we will later sub-sample: duskward, northward, downward and southward IMF. Key features related to our measurements are highlighted in purple (see main text).

267 For each convection map in Fig. 1, the magnetic pole is the centre of the map, dusk
 268 is towards the left, dawn towards right, midnight towards the bottom and noon towards
 269 the top. Colour-coded vectors show the SuperDARN line-of-sight measurements for each
 270 map. Black solid contours show the negative potential cells, which tend to lie on the dusk-
 271 side of the map and black dashed contours show the positive potential cells, which tend
 272 to lie on the dawn-side of the maps. In each map, some key features related to our mea-
 273 surements are highlighted in purple: The duskward IMF map and consecutive maps high-
 274 light the two foci of the negative and positive convection cells as purple \times and $+$, respec-
 275 tively. The contours surrounding the foci show the electrostatic potentials, which are equiv-
 276 alent to the convection cells. The number on the bottom right of each map, also high-
 277 lighted in purple shows the CPCP. On the northward IMF map in Fig.1, we have labelled
 278 the dusk- and dawn sides of the maps and we see that the negative and potential cells
 279 have now switched sides across the noon-meridian. This can be a key feature during north-
 280 ward, dawnward or duskward IMF. Later, we will explore the frequency at which this
 281 occurs. On the dawnward IMF convection pattern in Fig.1, we have highlighted the con-
 282 vection throat, where plasma flows from the dayside into the polar cap. We have not ex-
 283 plicitly extracted this feature, but it is an important morphological constraint which we
 284 will mention again. The map for southward IMF in Fig.1 illustrates the return flow re-
 285 gions. The purple arrows illustrate the width of the return flow regions of the negative
 286 and the positive convection cells.

287 Having extracted the aforementioned parameters as a timeseries from the Super-
 288 DARN convection maps, we condense the timeseries data into probability distribution
 289 functions (PDFs) for each parameter. First, we will compare the above mentioned pa-
 290 rameters from the negative to the positive potential cells for the D4 dataset to each other.
 291 This allows us to establish a general baseline of the asymmetries present.

292 We then further sub-sample the D4 dataset by high n ($n > 200$) and times when
 293 the solar wind clock angle is purely pointing northward ($0 \pm 15^\circ$), dawnward ($-90 \pm$
 294 15°), duskward ($90 \pm 15^\circ$) or southward ($180 \pm 15^\circ$). We look at these data for when
 295 these clock angle conditions are fulfilled for a short while ($\tau < 20$ minutes) and for a
 296 long time ($\tau > 300$ minutes). In either case, these conditions must be fulfilled at least
 297 90% of the time, which allows for very short solar wind deviations. This allows us to test
 298 for solar wind control of any asymmetries in the location and strength of the convection
 299 cells, as well as the importance of solar wind steadiness. Adding a limit for n reduces
 300 the reliability on the background model and thus allows us to isolate asymmetries that
 301 are a consequence of the solar wind conditions. We produce PDFs for these sub-sampled
 302 datasets which allows us to readily compare the different distributions.

Using PDFs, we then compare the parameters in datasets D1 and D3 with D4, the most modern set-up, which we use as our control dataset. We compare D1 and D4 to see how the historical dataset compares to the most modern set-up. A comparison between D3 to D4 allows us to see the effects on the convection maps of changing the background model only once all radars have been added. Our approach allows us to further investigate how the expansion of the network has changed the measured parameters by comparing the figures showing D1 versus D4 to D3 versus D4.

3 Results

Figure 2 a to d shows a summary of the asymmetries seen in the D4 dataset., which represents the modern SuperDARN set-up. Panel a shows the magnitudes of the negative against the positive potentials. More data lies below the line of unity (77%), as opposed to above (22%) which means the negative potential cell is more likely to be stronger. Panel b shows the return flow width of the negative and positive potential cells against each other, which show no discernible asymmetry (53% of data lie below the line of unity and 46% lie above the line of unity). Panel c show the cell foci's latitudes plotted against each other. These show some clear asymmetries. The distribution of data is skewed towards the the top of the plot, which means the positive potential cell is more likely to be located near the geomagnetic pole. Overall, 47% of the data lie above the line of unity (i.e. the positive potential cell focus is closer to the geomagnetic pole), and 42% of data lie below the line of unity (i.e. the negative potential cell focus is closer to the geomagnetic pole). The remaining 11% lie on the line of unity. Panel d shows the MLT locations of the negative and positive potential cell foci plotted against each other. Here we have defined the the MLT position as $MLT^*=24-MLT$ for the negative focus, such that the asymmetries are easily spotted. We see that the MLT location of the foci is also skewed: The negative cell focus has more data concentrated at lower MLT values (0 to 10 MLT^* has 97% of the x-axis data) than the positive cell focus at higher values (0 to 10 MLT has 93% of y-axis data). In other words the negative cell is most likely to be located in the evening sectors on the nightside, whereas the positive cell is most likely to be located in the early morning sectors (<10 MLT). Instances where both convection foci are located on the dayside ($6 < MLT < 18$) only comprise 8% of all data.

3.1 Sub-sampling by Solar Wind Conditions

Next, we will look at which asymmetries are controlled by solar wind conditions. For this analysis, we use a sub-sample of the D4 dataset, where $n > 200$ only, which allows us to ensure that the influence of the background model is minimised (Walach et al., 2022). This leaves us with 25% of the total data. We further split this data into times when the solar wind had a steady clock angle for up to 20 minutes (short τ) and for more than 300 minutes (long τ). We consider clock angles for southward IMF (clock angle= $180^\circ \pm 25^\circ$), northward IMF (clock angle= $0^\circ \pm 25^\circ$), dawnward IMF (clock angle= $-90^\circ \pm 25^\circ$) and duskward IMF (clock angle= $90^\circ \pm 25^\circ$). Figure 3 and 4 show these data as PDFs. The left column shows short τ and the right column shows long τ . Different colours indicate the different solar wind conditions, where dark blue shows southward IMF, light blue shows northward IMF, green shows dawnward IMF and yellow shows duskward IMF. In each case, the lower (25%) and upper (75%) quartiles are highlighted by the coloured blocks and the vertical lines show the medians.

Panels a and b, and c and d in Fig.3 show the negative and positive potential, respectively. Panels a to d show generally that both potential cells are weakest for northward IMF and strongest for southward IMF, followed by duskward IMF for the negative potential and dawnward for the positive potential cell. The IMF B_z and solar wind velocity distributions for the dawnward and duskward IMF are examined further in Figure SI1, which shows that they can be considered similar for dawnward and duskward

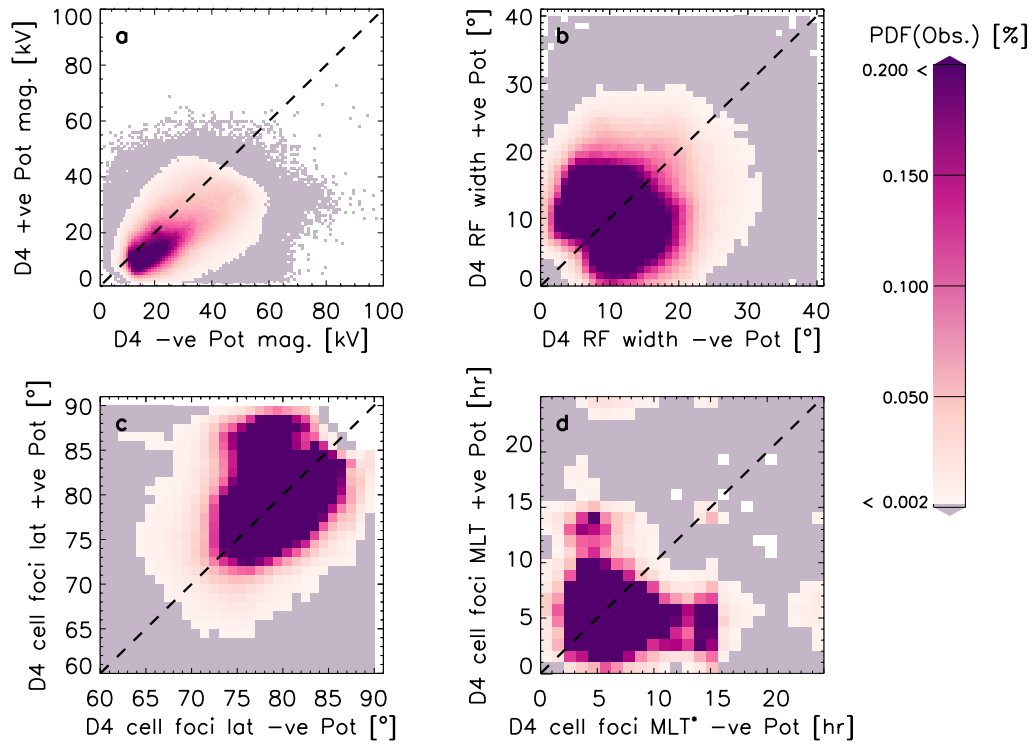


Figure 2. Panels a to d show a summary of asymmetries for D4. Panels a to d show the data from the negative cells against the data from the positive cells for the potential strength, the return flow width, the latitudinal location of the cell foci, and the MLT location of the cell foci ($MLT^*=24-MLT$), respectively.

353 IMF in each case. For long τ and southward IMF, we see the dark blue medians moved
 354 from -29 to -56kV (panels a to b) and 25 to 41kV (panels c to d). For northward IMF
 355 the distributions do not change much when the IMF timescale changes from short to long
 356 τ , but the differences between duskward and dawnward distributions become more pro-
 357 nounced for long τ . In all cases, the negative potentials' magnitudes are larger than the
 358 positive potentials', which means the negative potential cell holds more of the convec-
 359 tive flow. Panels e, f, g and h in Fig.3 show the return flow width for the negative and
 360 positive potential cells. Panel e shows that all four IMF distributions are similar for the
 361 short τ . All medians are between 10 and 14°, which is contrasted by the long τ distri-
 362 butions shown in panel f: Now the dark blue distribution for southward IMF has widened
 363 and the median is now highest (above 18°). The return flow width for duskward IMF
 364 is the second most likely to be wider than in panel e (above 17°), whereas the distribu-
 365 tions for dawnward and northward IMF barely change from short τ to long τ . Panel g
 366 shows the return flow width for the positive potential cell and short τ . The distributions
 367 for short τ shown here are very similar to panel e above, except for dawnward IMF for
 368 which the median is shifted higher by a few degrees (to around 14°, as opposed to 11°).
 369 Whilst the change for dawnward IMF is fairly minimal, for southward IMF we see a more
 370 considerable change. For long τ (panel h), the southward IMF distribution has again shifted
 371 to the right (median at 28°), which means we are more likely to observe a wider return
 372 flow width of the positive potential cell during southward IMF.

373 The analysis which follows in Figure 4 is a continuation of Fig. 3. Fig. 4 panels
 374 a to d summarise the latitudinal location of the cell foci and panels e to h summarise
 375 the MLT location of the cell foci. Panels a and c show that the latitudinal locations of
 376 the cell foci are similar, though duskward IMF drives the negative potential cell focus
 377 much closer to the magnetic pole (panel a, yellow distribution) than any of the other dis-
 378 tributions in panel a. In panel b, the yellow distribution is less further to the right of the
 379 plot, which means that for dawnward IMF the negative potential cell focus lies closer
 380 to the magnetic pole. The median of the yellow distribution in panel c is at 77°, whereas
 381 in panel a, it was at 79°. For long periods of duskward IMF, this pattern becomes more
 382 obvious: the negative potential cell's focus is located nearest to the pole. We see that
 383 in panel b all the other distributions have spread out too: the negative potential cell fo-
 384 cus's latitudinal position for long periods of northward IMF has a median of 79°, for long
 385 periods of dawnward IMF the median is 76° and for southward IMF it has moved equa-
 386 torward from 78° for short τ to 74°. In panel c, the distributions are much closer bunched
 387 together, such that they are almost indistinguishable. The distribution for the dawnward
 388 IMF conditions (in yellow) now has a median of 78° as opposed to 82° in panel a. Com-
 389 paring panels c and d, the distributions stay largely the same, except for southward IMF
 390 where the cell focus moves closer to the pole as the median moves from 77° for short τ
 391 to 68° for long τ . Overall, both cell foci lie furthest away from the pole for long τ dur-
 392 ing southward IMF.

393 Panels e to h show the MLT location of the convection cell foci. Panel e shows that
 394 most of the negative potential foci lie between 15 and 21 hrs, irrelevant of solar wind condi-
 395 tions. Panel f shows that for longer τ this is still the case, but we also see a secondary
 396 peak in the northward IMF and duskward IMF foci near 10 MLT. This secondary peak
 397 is also existent in panel e, but it becomes more obvious in panel f than e, as a larger pro-
 398 portion of the cell foci sit near 10 MLT. The positive potential cell foci's MLT location
 399 is similarly steady under different solar wind conditions: For both panels g and h, the
 400 majority of all distributions fall between 3 and 8 hrs. We also see a secondary peak around
 401 13 MLT, but only for northward IMF.

402 3.2 Sub-sampling by Dataset

403 Figure 5 a to c show the PDFs of the negative potential for D1 and D3 against D4
 404 and D3 where $n > 200$ against D4 where $n > 200$ and panels d to f show the equivalent pos-

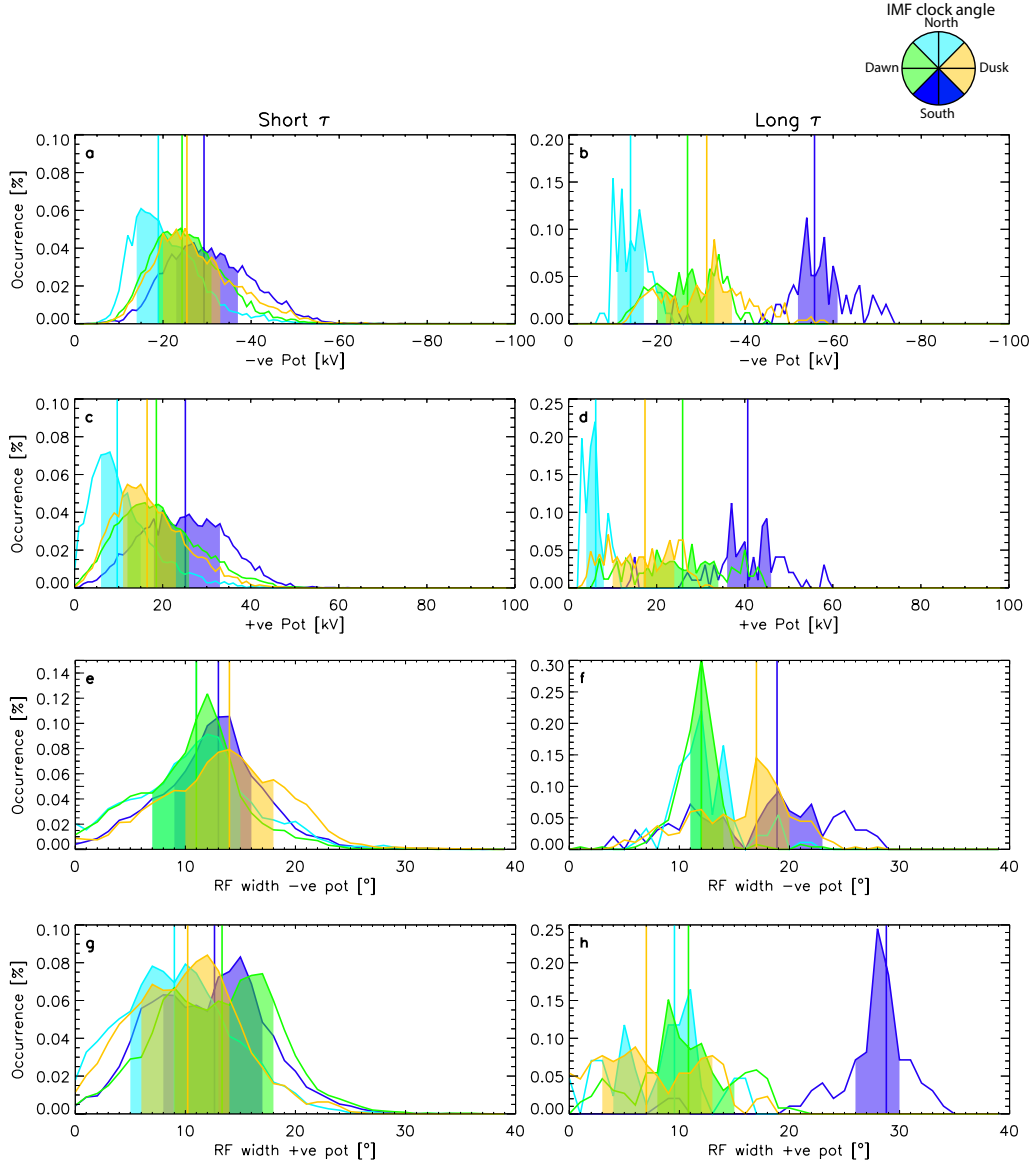


Figure 3. Panels a to h show PDFs of D4 where $n > 200$ and the clock angle was steady for a given amount of time, the rows show different parameters (negative potential, positive potential, return flow width of the negative and positive potential cells), and each column shows the sub-sample of the data corresponding to different steadiness timescales: up to 20 minutes (left) and more than 300 minutes (right column). The different coloured PDFs correspond to varying solar wind conditions: southward IMF ($-155^\circ \leq \text{clock angle} < 155^\circ$) in dark blue; northward IMF ($-25^\circ \leq \text{clock angle} < 25^\circ$) in light blue; dawnward IMF ($-115^\circ \leq \text{clock angle} < -65^\circ$) in green; duskward IMF ($65^\circ \leq \text{clock angle} < 115^\circ$) in yellow. The coloured blocks indicate the majority of the data, bounded by the lower (25%) and upper (75%) quartiles. The vertical lines indicate the medians of each distribution.

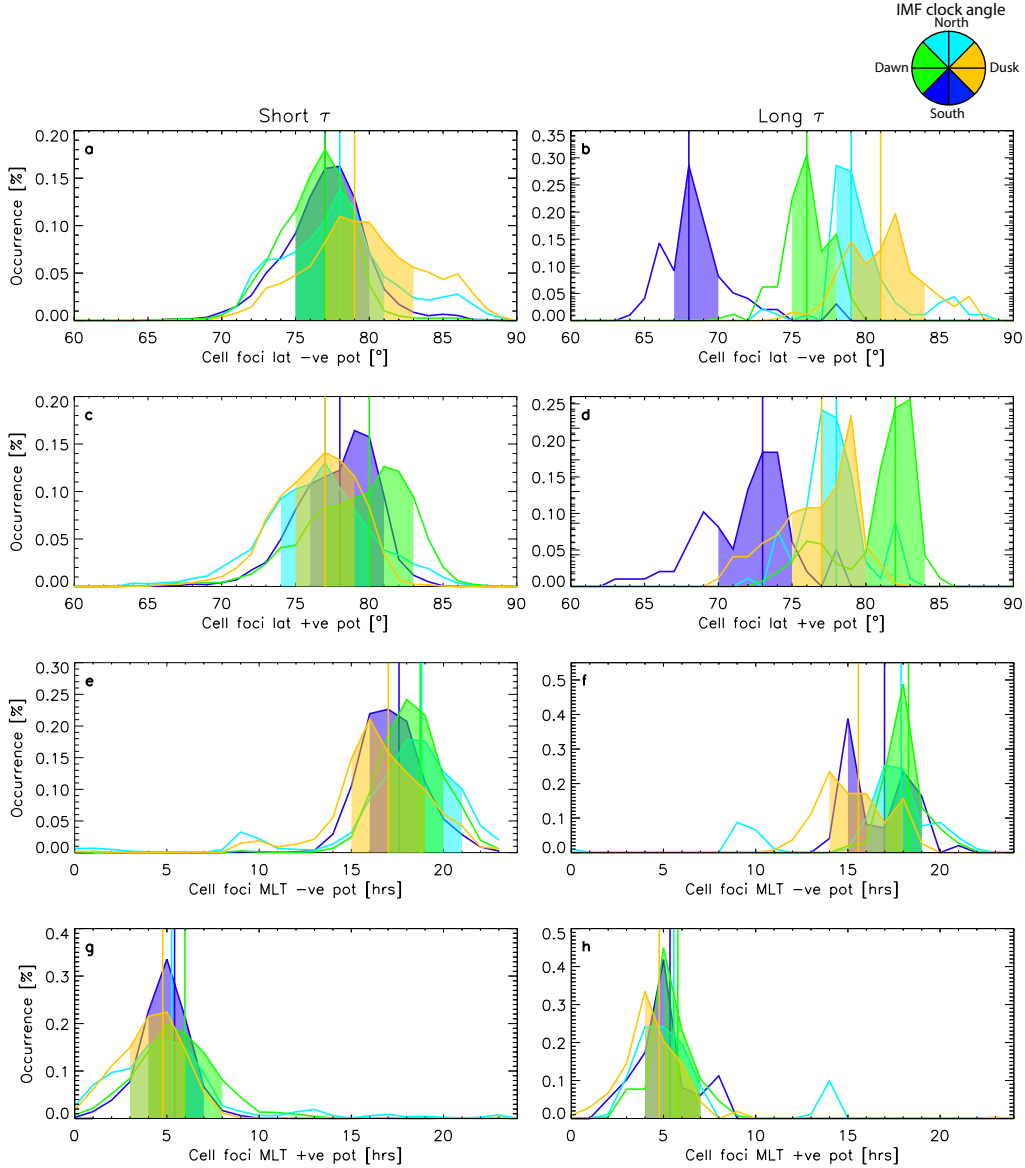


Figure 4. Panels a to h show PDFs of D4 where $n > 200$ and the clock angle was steady for a given amount of time. The rows show different parameters which describe the cell foci locations (latitude of negative cell foci, latitude of positive cell foci, MLT of negative potential cell foci and MLT of positive potential cell foci), and each column shows the sub-sample of the data corresponding to different steadiness timescales: up to 20 minutes (left) and more than 300 minutes (right column). The different coloured PDFs correspond to varying solar wind conditions: southward IMF ($-155^\circ > \text{clock angle} > 155^\circ$) in dark blue; northward IMF ($-25^\circ \leq \text{clock angle} < 25^\circ$) in light blue; dawnward IMF ($-115^\circ \leq \text{clock angle} > -65^\circ$) in green; duskward IMF ($65^\circ \leq \text{clock angle} > 115^\circ$) in yellow. The coloured blocks indicate the majority of the data, bounded by the lower (25%) and upper (75%) quartiles. The vertical lines indicate the medians of each distribution.

405 itive potential distributions. For D1 (panels a, and d), the negative cell is generally stronger
 406 than the positive, which creates an asymmetry in the convection pattern. The magni-
 407 tude of both potentials primarily fall within the 0 to 40 kV range. For panels a and d,
 408 94% and 99% of the D1 data, respectively fall below 40kV magnitude. When we con-
 409 sider which proportion of the data for D1 and D4 falls within the 0 to 40 kV magnitude
 410 range, this becomes a smaller portion of the data, but it is still the overwhelming ma-
 411 jority with 85% and 98%, respectively. In panels b and e, once the entire radar network
 412 is included and we compare D3 to D4, the potential strength increases for the negative
 413 potential cell (93% of the D3 dataset are now at magnitudes below 40kV). When we in-
 414 troduce a backscatter echo threshold of 200 (most righthand column), we expect the con-
 415 vection maps to rely less on the background model and to thus be more reliable. We see
 416 this take an effect when we compare panels a,b, and d and e to panels c, and f, respec-
 417 tively: The RG96 background model quantizes and we see vertical striations in the elec-
 418 trostatic potential. This is due to not enough data being available and the data process-
 419 ing thus relies strongly on the background model. These vertical striations were also de-
 420 tected by Walach et al. (2022) in the CPCP, who attributed this to the discrete binning
 421 in the RG96 model. This can also be seen to some extent in panels b and e here, though
 422 the effect is less obvious when all radars are included due to improved data coverage. When
 423 we compare panels a and d to panels c and f, the quantization effect disappears entirely.
 424 TS18 linearly interpolates between model bins, so the effect is not existent in the hor-
 425 izontal direction in any of panels a to f. Panels g to i show the PDFs of the return flow
 426 width for the negative potential cell and panels j to l show the equivalent for the pos-
 427 itive potential cell. Generally, the return flow width shows little dependence on the back-
 428 ground model but data coverage is important. Panels g and j show that the return flow
 429 width for both cells is always less than 30° for D1 in comparison to D4, which spans the
 430 full 40° range. This is due to the limited radar coverage in the D1 dataset, as we observe
 431 the return flow width extending for D3 (panels h and k). Panels h and k show a reduced
 432 amount of scatter in comparison to g and j, which means the D3 return flow width is more
 433 likely to be more similar to D4's. Panels i and l have less scatter, which indicates that
 434 when data coverage is high, the return flow width becomes more stable, regardless of the
 435 background model used.

436 Figure 6 shows the PDFs for the latitudinal and MLT location of the negative and
 437 positive cell locations in the same format as Fig.5. Panels a and d show that the D4 lat-
 438 itudinal cell location is more variable in the D4 dataset than in D1 due to the data be-
 439 ing distributed in a fairly narrow band in the x-direction in comparison to the y-direction.
 440 Comparing panels a and d it seems that the positive cell is more likely to lie at lower lat-
 441 itudes than the negative cell as the scatter in the x-direction covers a wider range in panel
 442 d. If we consider the amount of convection cell foci which lie below 75° we conclude that
 443 this the case: In panel d, 18% of the D1 convection cell foci lie below 75° , whereas in panel
 444 a this is only 3%. If we consider what percentage of cell foci in D4 and D1 lie below 75° ,
 445 we find that this is 2% and 7% for the negative and positive potential cells, respectively.
 446 Panels b and e show the latitudinal location of the negative and positive potential cells
 447 for D3 against D4. In contrast to panels a and d, these show the range of the data ex-
 448 tending to lower latitudes in the x-direction. This is due to the D3 dataset including all
 449 radars, which means the improved data coverage allows the cell foci to be located at a
 450 wider variety of latitudes. The percentage of negative cell foci (panel b) which lie be-
 451 low 75° in D3 and D4 is at 8% and for positive cell foci (panel e), this is at 12%, so the
 452 balance is similar as for panels a and d where the negative cell foci are more likely to be
 453 located at a lower latitude. Panels c and f show the subset of these data, where $n > 200$.
 454 These show a reduced version of panels b and e but no clear differences are seen between
 455 panels c and f and panels b and e, which means the asymmetries in the cell foci's lat-
 456 itudinal location due to the background model are existent whether or not a data thresh-
 457 old is introduced. There would be no background model influence if all data was distributed
 458 on or near the line of unity. Panels g to l show the negative and positive cell foci's MLT
 459 location. Panel g shows a vertical stripe between 15 to 20 MLT, where 95% of the cell

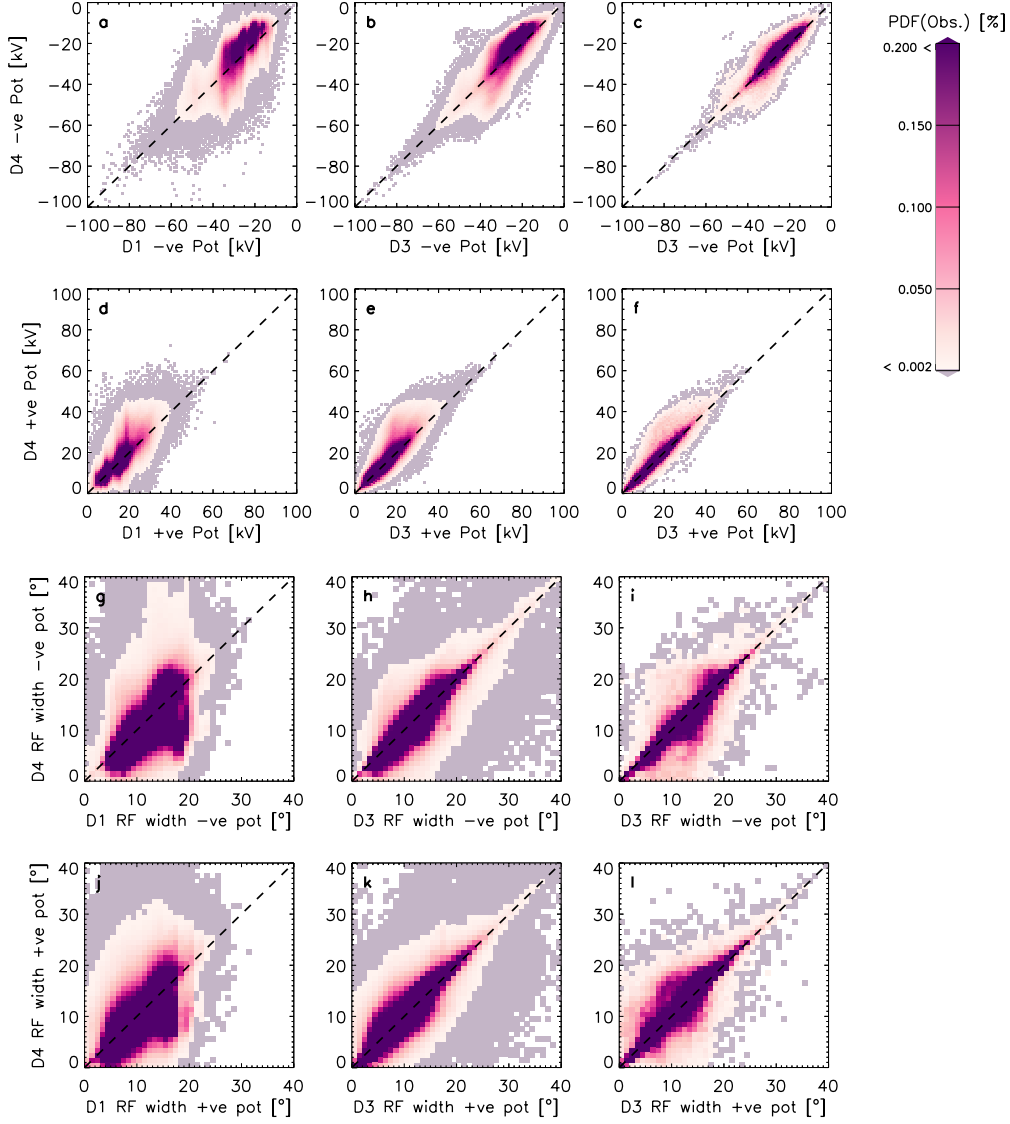


Figure 5. Panels a to c show the PDFs of the negative potential strength for D1, and D3 against D4, and D3 ($n > 200$) against D4 ($n > 200$). Panels d to f show the PDFs of the positive potential strength for D1, D3 against D4, and D3 ($n > 200$) against D4 ($n > 200$). Panels g to i show the PDFs of the return flow width for the negative potential cell for D1, D3 against D4, and D3 ($n > 200$) against D4 ($n > 200$). Panels j to l show the PDFs of the return flow width for the positive potential cell for D1, D3 against D4, and D3 ($n > 200$) against D4 ($n > 200$).

460 foci are located in the D1 dataset, whilst for D4 only 80% of data falls within this range.
 461 This tells us that there is a strong bias in the location with respect to the dataset. In
 462 panel h, the vertical stripe is reduced in comparison to panel g, which means introduc-
 463 ing more data has varied the MLT location of the negative cell foci. Now only 89% of
 464 the D3 cell foci's MLT location fall between 15 to 20 MLT. For panel i when a thresh-
 465 old of $n > 200$ is introduced, we see that the vertical structure reduces and instead be-
 466 comes a clear secondary peak at around 10 MLT. Interestingly, we do not see a symmet-
 467 ric peak in the D3 foci in panel i (i.e. in the top half of the plot), which means that al-
 468 though we have reduced the background model's influence, this asymmetry is inherent
 469 to the background model. Panels j to l show the foci's MLT location for the positive po-
 470 tential cell. These show different features to panels g to i, owing to the asymmetries shown
 471 in Fig. 2. In panel j, 97% of the D4 cell foci are located between 0 and 10 MLT, whereas
 472 for D1 this is almost all the data with 99%. We see again a vertical structure extend-
 473 ing up to 15 MLT, but also a weaker horizontal extension of the main peak at 5 MLT.
 474 In panel k, the main peak becomes more defined as 98% of cell foci in D3 are contained
 475 between 0 and 10 MLT, yet both the vertical and horizontal extension of the peak re-
 476 main. Panel l also shows a main peak in the cell foci's location contained between 0 and
 477 10 MLT: 96% of the D3 cell foci with $n > 200$ are located in this range. We also see fur-
 478 ther peaks between 15 and 20 MLT but these are less pronounced and occur for both
 479 D3 and D4. This is different to the secondary peak we saw in panel i, which is primar-
 480 ily existent in the D4 dataset. This means that sometimes the cell foci change MLT lo-
 481 cation from the main peak to the other side of the noon-midnight meridian, but this is
 482 more likely to occur for D4 than D3, which must be due to a bias in the background model.
 483 In Fig. 4 we saw that this predominantly occurs for northward and duskward IMF.

484 Figure 7 shows the asymmetries in the datasets. The column layout is the same
 485 as in Figs. 5 and 6 but each parameter now shows the differences between the positive
 486 and negative cells, so we can establish how the asymmetries vary. Panels a to c show the
 487 sum of the potentials (i.e. negative potential + positive potential). When this quantity
 488 is close to 0, the asymmetry between the negative and positive potentials is small. When
 489 this quantity is positive, the positive cell is dominating and when the sum is negative,
 490 the negative cell is dominating. Panel a shows that in both D1 and D4 the negative cell
 491 is mostly dominant. The large amount of scatter in panel a indicates that the asymme-
 492 tries are not necessarily correlated between D1 and D4. Panel b shows the potential strength
 493 asymmetries for D3 against D4. Here, the asymmetries are largely correlated with each
 494 other. The range of the spread is within ~ 20 kV from the line of unity, indicating that
 495 the background model accounts for approximately 20 kV in the variation of the asym-
 496 metry. Panel c shows the same comparison when only high n (> 200) maps are selected.
 497 Now the scatter has reduced but overall, the PDF is similar to panel b, which means the
 498 asymmetry differences between the two background models are not fully removed.

499 Panels d to f show the asymmetries in the return flow width (i.e. negative cell's width
 500 - positive cell's width). A negative value in these panels indicates that the positive cell's
 501 return flow region is wider than the negative cell's and vice versa. In panel d, 45% of the
 502 differences are positive for D1 and D4 and 35% are negative. This means that the nega-
 503 tive cell's return flow width is 10% more likely to be observed to be wider than the pos-
 504 itive cell's. This balance becomes slightly more pronounced in panel e, where 47% and
 505 36% of the values are positive and negative, respectively. Panel f shows a reduction in
 506 scatter in comparison to panel e, but the balance between asymmetries stays approxi-
 507 mately the same with 47% and 37% of values showing a positive and negative difference,
 508 respectively.

509 Panels g to i show the asymmetries in the latitudinal position of the cell foci (i.e.
 510 negative cell foci latitude - positive cell foci latitude). In panel g, most of the differences
 511 in D1 are clustered within $0 \pm 10^\circ$, which means the asymmetries in the foci locations are
 512 minimal in comparison to D4. In the y-direction of panel g, the asymmetries span the

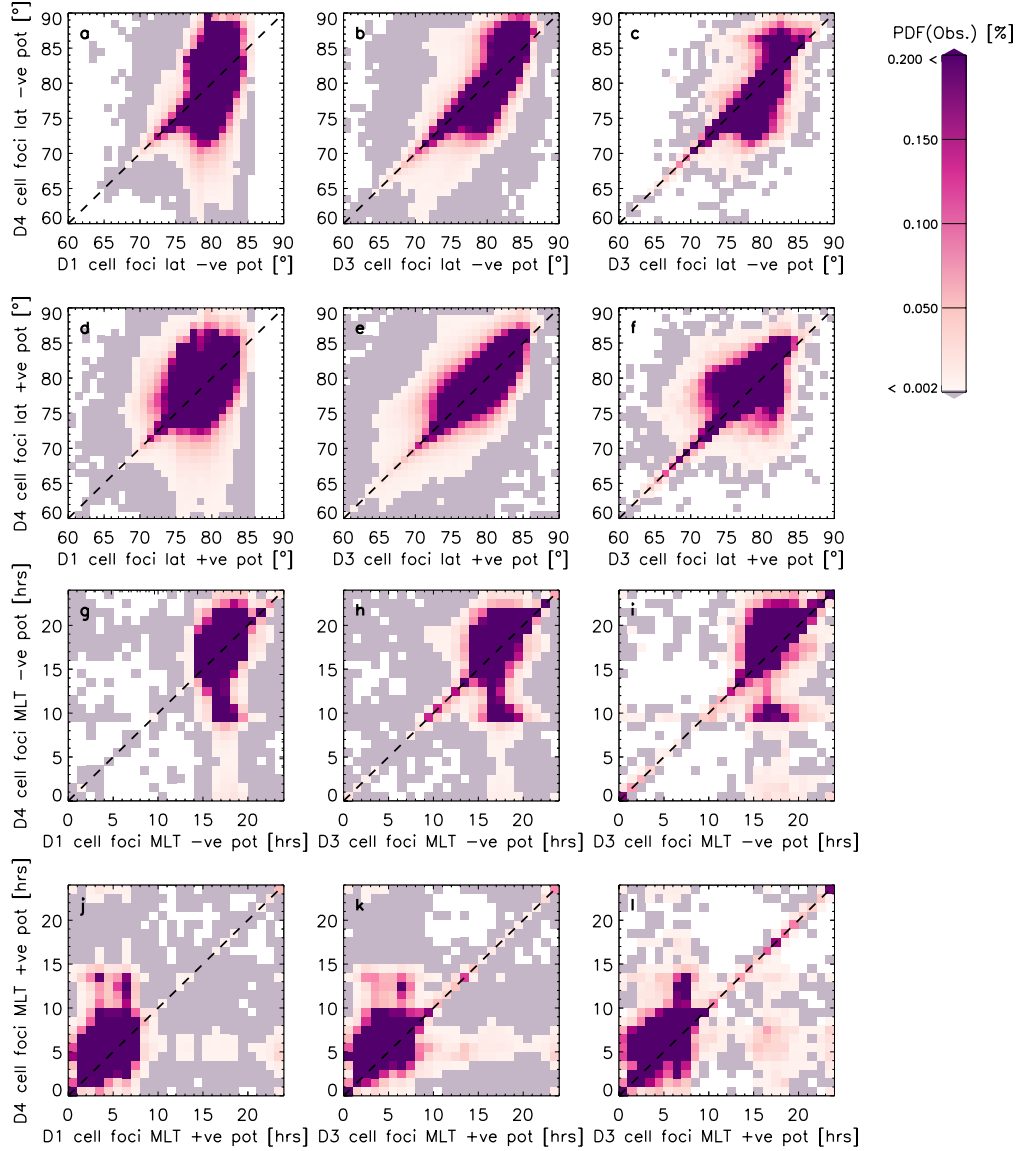


Figure 6. The columns are the same as in Fig.5: D3 against D4, and D3 ($n>200$) against D4 ($n>200$). Panels a to c show the PDFs of the negative potential latitude location. Panels d to f show the PDFs of the positive potential latitude location. Panels g to i show the PDFs of the negative potential's MLT location and panels j to l show the PDFs of the positive potential's MLT location.

entire $\pm 30^\circ$ range. Panel h shows that once all radars are introduced (D3), the data spreads a wide range in the x-direction also, adding to the asymmetry. In panel h we see that the asymmetries are roughly correlated with each other, but there is a large spread in values also. In panel i, where we have reduced the dataset, this spread is also reduced.

Panels j to l show the asymmetries in the MLT position of the cell foci (i.e. positive cell foci MLT* - negative cell foci MLT). A positive value here means the positive cell focus is further away from the noon meridian than the negative cell focus. Panel j shows a strong asymmetry in the cell foci's MLT positions for both D1 and D4, but perhaps less in the D1 than in the D4. In panel k, we see the asymmetries are more orientated near the line of unity. In panel l, the scatter has reduced but the main data structures remain the same as in panel k: a proportion of points are clustered above the line of unity near -5 and 10 hours in D4. This means that the background model is having an effect on the asymmetries, otherwise all points would lie near to the line of unity, especially when we select by high n only (panels in final column).

4 Discussion

Our observations have uncovered a number of dusk-dawn asymmetries in the SuperDARN convection maps. Overall, the magnitude of the negative potential cell tends to be stronger than the positive potential cell and the locations of cell foci are not symmetrically distributed. The asymmetries can largely be broken down into two groups: Asymmetries introduced by the background model and asymmetries due to solar wind control. We will now discuss the results in these contexts.

4.1 Asymmetries due to Solar Wind Control

We have shown that there are clear asymmetries in the negative and positive potentials when we select by high data threshold: the negative potential is stronger, and tends to lie at lower latitudes. Since this only becomes apparent when we select maps with a high n , it is suggestive of a systematic asymmetry which we attribute to solar wind control of the system. This is not a new observation and there is prior evidence for this: Walach and Grocott (2019) and Walach et al. (2021) showed that during geomagnetic storms for example, when the solar wind driving is particularly strong, the convection pattern moves generally to lower latitudes, and is asymmetric with the dusk cell being stronger, which in the case of a two-cell convection pattern is equivalent to the negative potential being stronger. Kumar et al. (2020) also showed that a strong IMF B_y component rotates the electrodynamic boundary between the dawn and dusk convection cells because they are linked via the field aligned current system to the ring current. They link this to alterations in the MLT distribution of ring current asymmetry, especially over timescales when the IMF B_y component is enhanced for ~ 12 hours or more. Since data for particularly long steady IMF periods, such as the $\tau \geq 12$ hours used by Kumar et al. (2020), are binned in our study together with shorter τ (≥ 5 hours), the cell foci's MLT locations are fairly similar for dawnward and duskward IMF.

Murr and Hughes (2007) also studied IMF conditions and their effects on ionospheric convection by examining the coherence between IMF measurements from the GEOTAIL mission and ionospheric equivalent flows derived from magnetometers. Murr and Hughes (2007) found that the coherence is higher for the North-South component and IMF B_z than the East-West convection component and the IMF B_y component. Overall, they also found that the coherence drops by a factor of three between the periods 32 and 21 min. We therefore expect convection responses to the solar wind to be more effective for short τ . We find however that the PDFs differ more for long τ than short τ , indicating that the large scale features in the convection pattern are more affected by longer τ IMF direction. Grocott and Milan (2014) also found that the convection asymmetries become more pronounced over longer timescales, but only when the IMF B_z is northward. Grocott

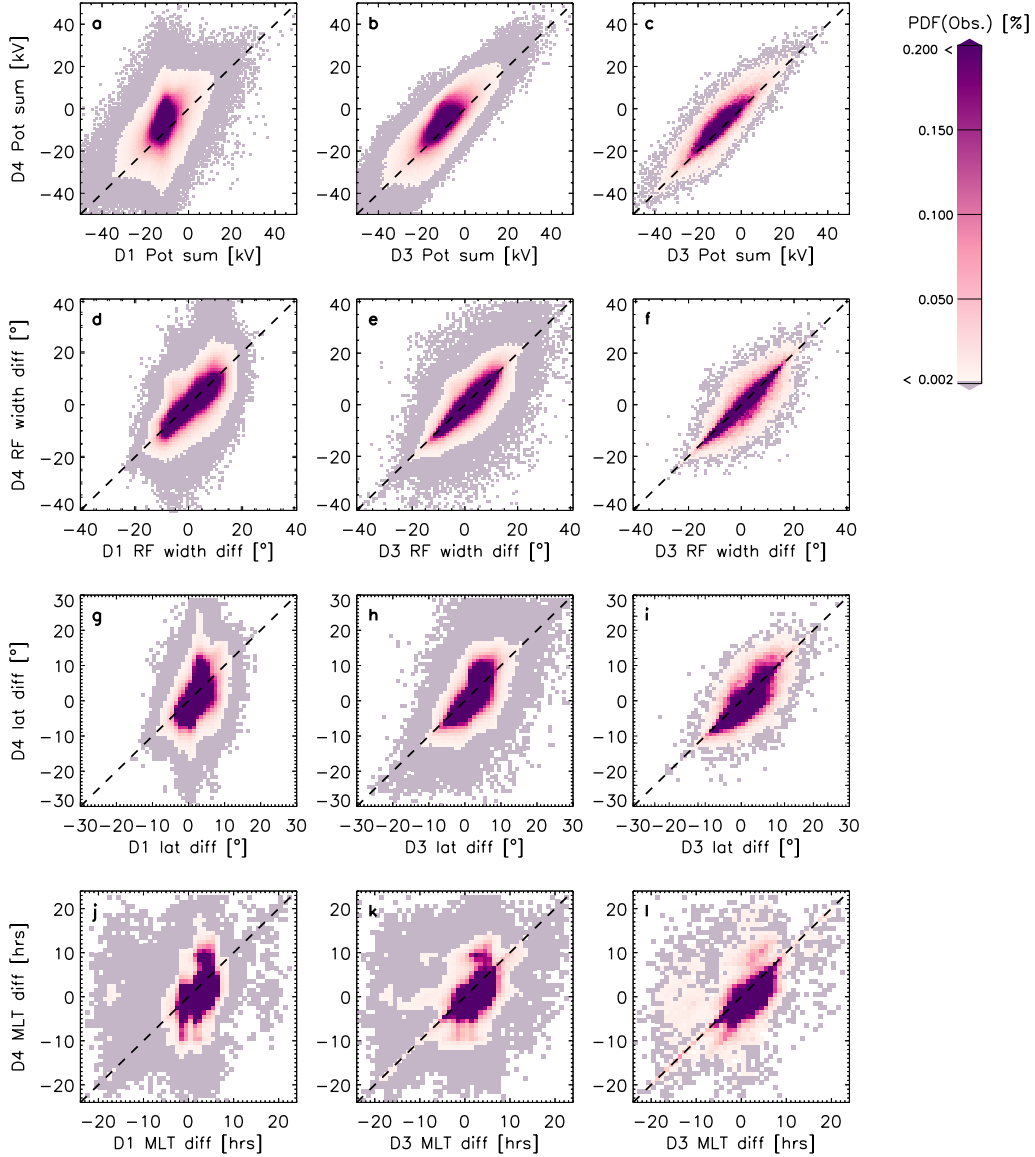


Figure 7. Panels a to c show the PDFs of the asymmetry in the potential (the sum of the -ve potential +ve potential, for D1, D3 and D3 where $n > 200$ against D4). Panels d to f show the PDFs of the asymmetry in the return flow width (the difference between the -ve cell width and the +ve cell width) for D1, D3 and D3 where $n > 200$ against D4. Panels g to i show the PDFs of the asymmetry in the the foci's latitudinal positions (the difference between the negative and positive cell foci's latitudinal positions) for D1, D3 and D3 where $n > 200$ against D4 and panels j to l show the PDFs of asymmetry in the foci's MLT positions (the difference between the positive cell foci's MLT* position and the negative foci's MLT position) for D1, D3 and D3 where $n > 200$ against D4.

563 and Milan (2014) find that the negative potential cell responds similarly to solar wind
 564 forcing, but the positive potential cell does not vary much in potential for dawnward IMF.
 565 We speculate that this is due to the differing methods used by Grocott and Milan (2014),
 566 who calculated average convection patterns. This discrepancy in results is likely due to
 567 the fact that Murr and Hughes (2007) only looked at the convection throat and we have
 568 studied parametrisations of the convection pattern overall.

569 When we filter our data further by solar wind conditions, the convection cells are
 570 strongest during southward, followed by dawn- or duskward IMF, depending on the cell.
 571 Our results largely agree with those from Grocott and Milan (2014), as we find that the
 572 negative potential cell becomes on average stronger for duskward IMF than dawnward
 573 IMF and the positive potential cell becomes on average stronger for dawnward IMF than
 574 duskward IMF (see Fig. 3). In this study this is more pronounced during longer inter-
 575 vals of steady IMF, whereas in Grocott and Milan (2014) only the negative potential cell
 576 increases strongly for long τ under duskward IMF. We further find that asymmetries in
 577 the location of the convection cells become particularly pronounced for northward and
 578 duskward IMF. When we filter the data for longer periods ($\tau > 300$ minutes) of steady
 579 IMF, the location of the positive potential tends to be at latitudes of 73° for southward
 580 IMF, whereas for dawnward IMF the location tends to be nearer to 82° . For duskward
 581 IMF, the positive potential tends to be at lower latitudes than the negative potential and
 582 vice versa during dawnward IMF. These results largely match with the findings of Grocott
 583 and Milan (2014), who used SuperDARN data to calculate the average convection pat-
 584 tern for different clock angles and IMF timescales: Grocott and Milan (2014) also found
 585 that for duskward IMF the positive potential tends to lie at lower latitudes than the neg-
 586 ative potential and vice versa for dawnward IMF. However, Grocott and Milan (2014)
 587 did not find that the convection pattern expands to as low latitudes as we did, but we
 588 know from Fig 6 (panels a and d) that this is due to the variation in analysis methods
 589 and to the fact that they used only data from 2000-2006, when no mid-latitude radars
 590 where built in the Northern hemisphere. The results from Grocott and Milan (2014) would
 591 be closer to our D1 results, which we have not split by solar wind conditions. Our re-
 592 sults make it clear that behind every average convection pattern, lies a multitude of pos-
 593 sibilities. When data is averaged together, the convection maps will most likely tend to
 594 favour higher latitudes, where backscatter is more likely to be observed due to better cov-
 595 erage by the radar network.

596 We find that the return flow width differs for the negative and positive potentials,
 597 when we select by solar wind conditions: it is clearly widest for southward IMF. This
 598 is not a surprise, as we expect convection to be stronger and span a larger range of lat-
 599 itudes during southward IMF, especially over longer timescales of steady IMF. Walach
 600 et al. (2021) for example showed that during the main phase of a storm in particular,
 601 when the IMF is southward, often for several hours, the return flow width becomes wider
 602 than usual. We find that the return flow width has little systematic asymmetry associ-
 603 ated with it and we postulate that this is due to the very symmetric HMB, which is used
 604 in the SuperDARN mapping. Whilst the dayside portion of the HMB is rotated slightly
 605 clockwise toward earlier local times and is thus slightly asymmetric, but this is accounted
 606 for as the convection cell foci are on average closer to the nightside than the dayside (see
 607 Fig. 2, panel d).

608 We find that for long periods of steady IMF, the negative and positive potentials
 609 can swap MLT sector, as they move from $\sim 0-9$ MLT to 14 MLT or $\sim 15-20$ MLT to 10
 610 MLT, which means the asymmetry in how far the average foci locations are from the noon-
 611 meridian is reduced as the swapping of MLT sectors for the positive and negative cells
 612 brings both potential locations to ± 2 hrs from noon. If the negative potential cell is lo-
 613 cated near dawn and the positive cell near dusk, the convection cells reverse. During long
 614 τ , we find that the largest asymmetry is now likely to be present under duskward IMF
 615 conditions, where the possibility of observing the potential focus location spans a large

616 range of MLT sectors. Unfortunately, it is not possible to establish a comparison between
 617 this result and those obtained by Grocott and Milan (2014) due to their study showing
 618 an average pattern for each solar wind condition. They do however find that when the
 619 IMF has been northward for a longer period of time, a four-cell pattern can establish,
 620 where a pair of reverse convection cells appears on the dayside at high latitudes due dual
 621 lobe reconnection, which closes open flux by reconnecting open field lines from the north-
 622 ern and southern hemispheres with each other (Russell, 1972; Burke et al., 1979; Reiff
 623 & Burch, 1985; Greenwald et al., 1995; Imber et al., 2007). These reverse convection cells
 624 usually appear superposed on top of the existing dual-cell convection pattern. During
 625 intervals of northward IMF with a B_y component, single lobe reconnection on open field
 626 lines produces a single convection cell in the polar cap (e.g. Russell, 1972; Jørgensen et
 627 al., 1972; S. Cowley, 1981b; Reiff & Burch, 1985; S. W. H. Cowley et al., 1991; Taylor
 628 et al., 1998; Imber et al., 2007). Both dual lobe or single lobe reconnection move the peak
 629 of the negative potential cell from dusk to dawn and vice versa (e.g. Reiff & Burch, 1985;
 630 Imber et al., 2007). We are unable to distinguish between the two mechanisms here, but
 631 we do see a clear correlation with the IMF direction. Imber et al. (2007) report: "dual
 632 lobe reconnection would be expected to cease when the clock angle exceeds $\pm 15^\circ$; at which
 633 point single lobe reconnection would be expected to recommence". This explains why
 634 we see the negative and positive potentials swap positions not only when the IMF is purely
 635 northward, but also when it is pointing dawn- or duskward, though during dawn- or duskward
 636 IMF it occurs preferentially for short IMF steadiness intervals.

637 Taylor et al. (1998) used SuperDARN and DMSP data to show that flow recon-
 638 figurations in the ionosphere associated with northward IMF can start to occur on short
 639 timescales (~ 2 min). This does however not necessarily mean a swapping of positions
 640 of the convection cell foci as these flows can be superposed on existing dual-cell convec-
 641 tion. Our statistics agree with the timescales shown by Taylor et al. (1998) and we show
 642 that the positional swapping of the convection cells can happen on short and long timescales
 643 of steady IMF, but is more likely to occur for longer τ . What is interesting is that the
 644 findings by Grocott and Milan (2014) show that the reverse convection cell only over-
 645 powers the dual convection cell after ~ 240 minutes. This would appear in our dataset
 646 as a positional swapping of the negative and positive cell foci in MLT sector, whereas
 647 we find that, statistically this can happen on shorter timescales too.

648 When we sub-sample D4 for $n > 200$ and solar wind conditions, we find that the
 649 two convection cells are most likely to swap sides (i.e. the MLT of the positive poten-
 650 tial focus is higher than the MLT of the negative potential focus) when the IMF is north-
 651 ward. When the IMF has been northward for a long interval (> 300 minutes), the po-
 652 sitional swap occurs $\sim 1.1\%$ of the time, whilst these IMF (long τ and northward IMF)
 653 and n conditions are fulfilled only 0.05% overall. For the short intervals of northward
 654 IMF shown in Fig. 4, this only occurs 4.1% of the time with the IMF conditions being
 655 significantly more likely to occur (IMF conditions are fulfilled 0.31% of overall dataset).
 656 This means that overall, the positional swap is 23 times more likely to be observed when
 657 the IMF is pointing northward for short τ . For long periods of duskward IMF, the two
 658 convection cells swap MLT sectors less often: this occurs 0.37% of the time, which is re-
 659 flected by the fact that these solar wind conditions are fulfilled more often (0.15% of the
 660 entire dataset). Short periods of duskward IMF are statistically much more likely to oc-
 661 cur ($\sim 0.42\%$ of all data) and yet, the convection cells are still not as likely to swap sides
 662 for these conditions as during northward IMF (0.95% of observable times).

663 This raises the question of how important the timescale of steady IMF is for the
 664 development of the reverse convection cell. In the past, different timescales have been
 665 reported for this. Imber et al. (2007) for example, observed the IMF clock angle pass-
 666 ing gradually from -180° to 0° to 180° over the course of 3 h, but they report that the
 667 clock angle has to be $\pm 15^\circ$ of northward IMF for dual lobe reconnection to occur. Sim-
 668 ilarly, Imber et al. (2006) estimated that the clock angle has to be $\pm 10^\circ$ for dual lobe

reconnection to occur, but Imber et al. (2007) shows that lobe reconnection can occur as soon as the IMF clock angle is pointing $\pm 15^\circ$. Here we have shown that the convection cells can swap sides on short and long timescales, but it preferentially occurs when the IMF has been northward for short periods of time due to the higher possibility of the IMF conditions being fulfilled.

4.2 Asymmetries due to the Background Model

Similar to the CPCP investigated by Walach et al. (2022), we see striations in the strength of the potential cells (mainly in D1 and less obviously in D3) for the maps created using the RG96 background model. These disappear when we change the background model to TS18 (D4) or only use maps with a high data threshold ($n > 200$). As already discussed in Walach et al. (2022) this is due to the RG96 model choosing discrete bins, which the fitting algorithm will rely on when little data is available.

We find that the MLT locations of the negative and positive potentials are not evenly distributed. That is to say, they are not mirrored around the noon meridian and do not cover an equal range of MLT values. Some of this will be due to innate asymmetries in the magnetosphere, as well as solar wind control, as discussed in the previous subsection (see also Walsh et al., 2014), but there is also an asymmetry due to the chosen background model. In particular, the negative potential's focus tends to be more confined to specific MLTs in D1 and D3, but can cover a large range of MLTs in D4, which manifests itself as larger asymmetries for D4 than D3 and D1. This means the RG96 model restricts the negative potential cell to a smaller range of MLTs than TS18. This is likely due to the fact that RG96 was developed with data from only one radar, whereas TS18 used 23 geographically distributed radars. In the convection pattern, this is likely to manifest itself as a fairly stable dusk cell with a more mobile dawn cell. We find that the convection cells swap sides (i.e. lobe-reconnection cells have established themselves) 0.6% of the time for D3 and 0.5% of the time for D4, irrespective of solar wind conditions. When we sub-sample D3 and D4 by $n > 200$, the convection cells swap sides 1.6% of the time for D3 and 1.4% of the time for D4. As the reverse cells only occur under specific solar wind conditions, we conclude that the bias in the convection cell placement manifests itself little for times when the convection cells are strongly dependent on the IMF. It is worth noting that whilst the background model can introduce a bias, it is generally less likely to do so when a large number of datapoints is available for the fitting. Although, indicating that whilst the background model can introduce a bias, it is generally less likely to do so when a large number of datapoints is available for the fitting. This is shown in the location in MLT of the convection cell foci which takes on a more discrete peak in the PDFs (Fig. 6). Figure 7 showed that this is due to a reduction in scatter and asymmetries which are brought about by the background model remain.

We further saw in Figure 7 that the asymmetries in the electrostatic potential are correlated with each other for D3 and D4 (for $n > 200$), indicating that these are driven by the data. Asymmetries in the positional placement of the foci however, remain when $n > 200$ is introduced, and they are not necessarily correlated for D3 and D4, which means there is an inherent bias in the background model.

In the average maps characterised by solar wind conditions shown by Grocott and Milan (2014), the IMF control shows that even when the IMF clock angle is pointing duskward for a prolonged time, the dusk cell's potential is always higher than the dawn cell's. Whilst we find that the negative (dusk) cell tends to hold a higher potential on average, we find that it is possible for the dawn cell to hold a higher potential than the dusk cell. Interrogating our dataset, we find that for the dataset using the TS18 background model (D4), the positive potential is stronger than the negative potential $\sim 23\%$ of the time, whereas in D3 (which uses the RG96 background model), this only occurs in $\sim 10\%$ of the convection maps. This shows that there can be considerable asymmetries introduced by the

720 background model and depending which one is chosen, dusk-dawn asymmetries appear
721 to varying degrees.

722 5 Summary

723 In this paper we have shown that there are systemic dusk-dawn asymmetries seen
724 in SuperDARN convection maps. We have shown that these are due to a mixture of so-
725 lar wind control of the magnetosphere-ionosphere system and biases in the SuperDARN
726 background models.

727 Observations in the data due to asymmetries introduced through solar wind con-
728 trol:

- 729 • When the data is filtered by solar wind conditions, the convection potentials are
730 strongest during southward and dusk- or dawnward IMF. The positive potential
731 cell is strongest during sustained periods of steady dawnward IMF, and the neg-
732 ative potential cell is strongest for sustained periods of steady duskward IMF. Asym-
733 metries in the location of the potential foci become particularly pronounced for
734 dawnward and duskward IMF.
- 735 • The negative and positive potential foci can swap positions for north-, dusk- and
736 dawnward IMF and both short and long periods of steady IMF, but it is most likely
737 to be observed when the IMF is northward for short periods of time.
- 738 • When the data is filtered for long periods (at least 300 minutes) of steady IMF,
739 the location of the positive potential can be at latitudes down to 60° for south-
740 ward IMF, whereas for dawnward IMF the location is contained to above 70° . For
741 duskward IMF, the positive potential tends to be at lower latitudes than the neg-
742 ative potential and vice versa during dawnward IMF.
- 743 • For long periods of steady IMF, when the reverse cells establish themselves, they
744 move from ~ 0 -9 MLT to 15 MLT or ~ 15 -23 MLT to 10 MLT, which means their
745 position with respect to 12 MLT reduces in asymmetry. The largest asymmetry
746 is now likely to be present under duskward IMF conditions, where we still see a
747 large spread away from the line of unity.
- 748 • The return flow width is similar for both the negative and positive potentials, un-
749 til we select by solar wind conditions, when the return flow region is clearly widest
750 for the negative potential under southward IMF.

751 Observations of asymmetries in the data due to background model:

- 752 • Clear asymmetries in negative versus positive potential when we select by a data
753 threshold ($n > 200$): the negative potential is stronger, and tends to lie at lower lat-
754 itudes.
- 755 • Striations in the strength of the potentials (primarily in the maps using the RG96
756 background model) due to discrete binning of the background model
- 757 • By comparing different background models and a data threshold ($n > 200$), we found
758 the background model used biased map potential fittings by influencing the RF
759 width, the location of the foci and strength of convection cell potentials.
- 760 • We found that introducing a data threshold does not eliminate the bias in the fit-
761 ting which introduces asymmetries in the foci locations.

762 Whilst we have shown general statistical results here, these uncovered asymmetries
763 may affect the conclusions drawn in statistical studies or individual case studies. In par-
764 ticular, we have shown that the SuperDARN background model affects the asymmetry
765 of the convection maps and this can to some extent be mitigated by sub-sampling the
766 dataset by using a minimal scatter-echo threshold. However, using a threshold does how-
767 ever not eliminate all asymmetries: The positional placement of the cell foci in partic-

ular exhibits asymmetries that are bias due to the background model. This result means that asymmetries presented in older SuperDARN studies (using the RG96 background model) could have been influenced by the background model.

Open Research

All data used for this study are available open source. The authors acknowledge the use of SuperDARN data. SuperDARN is a collection of radars funded by national scientific funding agencies of Australia, Canada, China, France, Italy, Japan, Norway, South Africa, United Kingdom, and United States of America, and we thank the international PI team for providing the data. The authors acknowledge access to the SuperDARN database via the British Antarctic Survey (<https://www.bas.ac.uk/project/superdarn/#data>). Other data mirrors are hosted by the Virginia Tech SuperDARN group (<http://vt.superdarn.org/>) and the University of Saskatchewan (<https://superdarn.ca/data-download>). The Radar Software Toolkit (RST) to process the SuperDARN data can be downloaded from Zenodo (<https://doi.org/10.5281/zenodo.1403226> and references). All solar wind data used to process the data were downloaded from NASA's SPDF Coordinated Data Analysis Web (<https://cdaweb.gsfc.nasa.gov/index.html/>). The processed data used for this publication is available under the DOI:10.17635/lancaster/researchdata/571 (Walach, 2022).

Acknowledgments

The authors thank the SuperDARN PIs for their continued work in making SuperDARN data available and the SuperDARN Data Analysis Working Group in their ongoing efforts to improve the software quality and accessibility. M.-T. W. and A. G. were supported by Natural Environments Research Council (NERC), UK, grant nos. NE/P001556/1 and NE/T000937/1. FF.S. was supported by NASA grants 80NSSC20K1402, 80NSSC20K1281, and NSF grant 2149782. E. G. T. thanks the National Science Foundation (NSF) for support under grants AGS-1934997. We gratefully acknowledge the use of Lancaster University's High End Computing Cluster, which has facilitated the necessary dataprocessing for this study.

References

- Atkinson, G., & Hutchison, D. (1978). Effect of the day night ionospheric conductivity gradient on polar cap convective flow. *Journal of Geophysical Research: Space Physics*, *83*(A2), 725-729. Retrieved from <https://agupubs.onlinelibrary.wiley.com/doi/abs/10.1029/JA083iA02p00725> doi: <https://doi.org/10.1029/JA083iA02p00725>
- Burke, W., Kelley, M., Sagalyn, R., Smiddy, M., & Lai, S. (1979). Polar cap electric field structures with a northward interplanetary magnetic field. *Geophysical Research Letters*, *6*(1), 21-24. doi: 10.1029/GL006i001p00021
- Chisham, G., Lester, M., Milan, S. E., Freeman, M. P., Bristow, W. A., Grocott, A., ... Walker, D. M. (2007). A decade of the Super Dual Auroral Radar Network (SuperDARN): Scientific achievements, new techniques and future directions. *Surveys in Geophysics*, *28*(1), 33-109. doi: 10.1007/s10712-007-9017-8
- Chisham, G., Yeoman, T. K., & Sofko, G. J. (2008). Mapping ionospheric backscatter measured by the superdarn hf radars – part 1: A new empirical virtual height model. *Annales Geophysicae*, *26*(4), 823-841. doi: 10.5194/angeo-26-823-2008
- Cousins, E. D. P., & Shepherd, S. G. (2010). A dynamical model of high-latitude convection derived from superdarn plasma drift measurements. *Journal of Geophysical Research: Space Physics*, *115*(A12). Retrieved from <https://agupubs.onlinelibrary.wiley.com/doi/abs/10.1029/2010JA016017> doi: 10.1029/2010JA016017

- 817 Cowley, S. (1981b). Magnetospheric and ionospheric flow and the interplanetary
818 magnetic field. *In AGARD The Phys. Basis of the Ionosphere in the Solar-*
819 *Terrest. System 14 p (SEE N81-23507 14-42).*
- 820 Cowley, S. W. (1981a). Magnetospheric asymmetries associated with the y-
821 component of the IMF. *Planetary and Space Science*, 29(1), 79–96. doi:
822 10.1016/0032-0633(81)90141-0
- 823 Cowley, S. W. H. (1982). The Causes of Convection in the Earth’s Magnetosphere:
824 A Review of Developments During the IMS. *Reviews of Geophysics and Space*
825 *Physics*, 20(3), 531–565. doi: 10.1029/RG020i003p00531
- 826 Cowley, S. W. H. (2000). Magnetosphere-ionosphere interactions: A tutorial review.
827 *Magnetospheric Current Systems, Geophys. Monogr. Ser.*, 118, 91–106. doi: 10
828 .1029/GM118p0091
- 829 Cowley, S. W. H., & Lockwood, M. (1992). Excitation and decay of solar wind-
830 driven flows in the magnetosphere-ionosphere system. *Annales geophysicae*, 10,
831 103–115.
- 832 Cowley, S. W. H., & Lockwood, M. (1996). Time-dependent flows in the coupled
833 solar wind-magnetosphere-ionosphere system. *Advances in Space Research*,
834 18(8), 141–150. doi: 10.1016/0273-1177(95)00972-8
- 835 Cowley, S. W. H., Morelli, J. P., & Lockwood, M. (1991). Dependence of convective
836 flows and particle precipitation in the high-latitude dayside ionosphere on the
837 x and y components of the interplanetary magnetic field. *Journal of Geophysi-*
838 *cal Research: Space Physics*, 96(A4), 5557–5564. doi: 10.1029/90JA02063
- 839 Forsythe, V. V., & Makarevich, R. A. (2017). Global view of the e region irreg-
840 ularity and convection velocities in the high-latitude southern hemisphere.
841 *Journal of Geophysical Research: Space Physics*, 122(2), 2467–2483. Retrieved
842 from [https://agupubs.onlinelibrary.wiley.com/doi/abs/10.1002/](https://agupubs.onlinelibrary.wiley.com/doi/abs/10.1002/2016JA023711)
843 [2016JA023711](https://doi.org/10.1002/2016JA023711) doi: <https://doi.org/10.1002/2016JA023711>
- 844 Foster, J. C., & Vo, H. B. (2002). Average characteristics and activity dependence
845 of the subauroral polarization stream. *Journal of Geophysical Research: Space*
846 *Physics*, 107(A12). doi: 10.1029/2002JA009409
- 847 Freeman, M., Ruohoniemi, J., & Greenwald, R. (1991). The determination of time-
848 stationary two-dimensional convection patterns with single-station radars.
849 *Journal of Geophysical Research: Space Physics*, 96(A9), 15735–15749. doi:
850 10.1029/91JA00445
- 851 Freeman, M. P. (2003). A unified model of the response of ionospheric convection to
852 changes in the interplanetary magnetic field. *Journal of Geophysical Research:*
853 *Space Physics*, 108(A1), 1–13. doi: 10.1029/2002JA009385
- 854 Greenwald, R. A., Baker, K. B., Dudeney, J. R., Pinnock, M., Jones, T. B., Thomas,
855 E. C., ... Yamagishi, H. (1995). Darn/superdarn. *Space Science Reviews*,
856 71(1), 761–796. doi: 10.1007/BF00751350
- 857 Grocott, A., Cowley, S., Sigwarth, J., Watermann, J., & Yeoman, T. K. (2002).
858 Excitation of twin-vortex flow in the nightside high-latitude ionosphere
859 during an isolated substorm. *Annales Geophysicae*, 20, 1577–1601. doi:
860 10.5194/angeo-20-1577-2002
- 861 Grocott, A., Cowley, S. W. H., & Sigwarth, J. B. (2003). Ionospheric flow during
862 extended intervals of northward but By-dominated IMF. *Annales Geophysicae*,
863 21(2), 509–538. doi: 10.5194/angeo-21-509-2003
- 864 Grocott, A., Laurens, H. J., & Wild, J. A. (2017). Nightside ionospheric convec-
865 tion asymmetries during the early substorm expansion phase: Relationship
866 to onset local time. *Geophysical Research Letters*, 44(23), 11,696–11,705.
867 Retrieved from [https://agupubs.onlinelibrary.wiley.com/doi/abs/](https://agupubs.onlinelibrary.wiley.com/doi/abs/10.1002/2017GL075763)
868 [10.1002/2017GL075763](https://doi.org/10.1002/2017GL075763) doi: <https://doi.org/10.1002/2017GL075763>
- 869 Grocott, A., & Milan, S. E. (2014). The influence of imf clock angle timescales
870 on the morphology of ionospheric convection. *Journal of Geophysical Research:*
871 *Space Physics*, 119(7), 5861–5876. doi: 10.1002/2014JA020136

- 872 Grocott, A., Milan, S. E., Imber, S. M., Lester, M., & Yeoman, T. K. (2012). A
 873 quantitative deconstruction of the morphology of high-latitude ionospheric con-
 874 vection. *Journal of Geophysical Research: Space Physics*, *117*(A5). Retrieved
 875 from [https://agupubs.onlinelibrary.wiley.com/doi/abs/10.1029/](https://agupubs.onlinelibrary.wiley.com/doi/abs/10.1029/2012JA017580)
 876 [2012JA017580](https://agupubs.onlinelibrary.wiley.com/doi/abs/10.1029/2012JA017580) doi: 10.1029/2012JA017580
- 877 Grocott, A., Milan, S. E., & Yeoman, T. K. (2008). Interplanetary magnetic field
 878 control of fast azimuthal flows in the nightside high-latitude ionosphere. *Geo-*
 879 *physical Research Letters*, *35*(L08102). doi: 10.1029/2008GL033545
- 880 Haaland, S. E., Paschmann, G., Förster, M., Quinn, J. M., Torbert, R. B., McIlwain,
 881 C. E., ... Kletzing, C. A. (2007). High-latitude plasma convection from cluster
 882 edi measurements: method and imf-dependence. *Annales Geophysicae*, *25*(1),
 883 239–253. Retrieved from [https://angeo.copernicus.org/articles/25/239/](https://angeo.copernicus.org/articles/25/239/2007/)
 884 [2007/](https://angeo.copernicus.org/articles/25/239/2007/) doi: 10.5194/angeo-25-239-2007
- 885 Heppner, J. P., & Maynard, N. C. (1987). Empirical high-latitude electric field
 886 models. *Journal of Geophysical Research*, *92*(A5), 4467–4489. doi: 10.1029/
 887 [JA092iA05p04467](https://doi.org/10.1029/JA092iA05p04467)
- 888 Imber, S. M., Milan, S. E., & Hubert, B. (2006). The auroral and ionospheric flow
 889 signatures of dual lobe reconnection. *Annales Geophysicae*, *24*(11), 3115–3129.
 890 Retrieved from <https://angeo.copernicus.org/articles/24/3115/2006/>
 891 [doi: 10.5194/angeo-24-3115-2006](https://angeo.copernicus.org/articles/24/3115/2006/)
- 892 Imber, S. M., Milan, S. E., & Hubert, B. (2007). Observations of significant flux clo-
 893 sure by dual lobe reconnection. *Annales Geophysicae*, *25*(7), 1617–1627. doi:
 894 [10.5194/angeo-25-1617-2007](https://doi.org/10.5194/angeo-25-1617-2007)
- 895 Jørgensen, T. S., Friis-Christensen, E., & Wilhjelm, J. (1972). Interplanetary
 896 magnetic-field direction and high-latitude ionospheric currents. *Journal of*
 897 *Geophysical Research*, *77*(10), 1976–1977. doi: 10.1029/JA077i010p01976
- 898 Kumar, S., Veenadhari, B., Chakrabarty, D., Tulasi Ram, S., Kikuchi, T., &
 899 Miyoshi, Y. (2020). Effects of imf by on ring current asymmetry under south-
 900 ward imf bz conditions observed at ground magnetic stations: Case studies.
 901 *Journal of Geophysical Research: Space Physics*, *125*(10), e2019JA027493.
 902 Retrieved from [https://agupubs.onlinelibrary.wiley.com/doi/abs/](https://agupubs.onlinelibrary.wiley.com/doi/abs/10.1029/2019JA027493)
 903 [10.1029/2019JA027493](https://agupubs.onlinelibrary.wiley.com/doi/abs/10.1029/2019JA027493) (e2019JA027493 2019JA027493) doi: [https://doi.org/](https://doi.org/10.1029/2019JA027493)
 904 [10.1029/2019JA027493](https://doi.org/10.1029/2019JA027493)
- 905 Lockwood, M., & Morley, S. K. (2004). A numerical model of the ionospheric sig-
 906 natures of time-varying magnetic reconnection : I . ionospheric convection. *An-*
 907 *nales Geophysicae*, *22*, 73–91. doi: 10.5194/angeo-22-73-2004
- 908 Milan, S. E., Clausen, L. B. N., Coxon, J. C., Carter, J. A., Walach, M.-T., Laundal,
 909 K., ... Anderson, B. J. (2017). Overview of solar wind–magnetosphere–
 910 ionosphere–atmosphere coupling and the generation of magnetospheric cur-
 911 rents. *Space Science Reviews*, *206*(1), 547–573. Retrieved from [https://](https://doi.org/10.1007/s11214-017-0333-0)
 912 doi.org/10.1007/s11214-017-0333-0 doi: 10.1007/s11214-017-0333-0
- 913 Murr, D., & Hughes, W. (2007). The coherence between the imf and high-latitude
 914 ionospheric flows: The dayside magnetosphereionosphere low-pass filter.
 915 *Journal of Atmospheric and Solar-Terrestrial Physics*, *69*(3), 223–233. Re-
 916 trieved from [https://www.sciencedirect.com/science/article/pii/](https://www.sciencedirect.com/science/article/pii/S1364682606002628)
 917 [S1364682606002628](https://www.sciencedirect.com/science/article/pii/S1364682606002628) (Global Aspects of Magnetosphere-Ionosphere Coupling)
 918 doi: <https://doi.org/10.1016/j.jastp.2006.07.019>
- 919 Nishitani, N., Ruohoniemi, J. M., Lester, M., Baker, J. B. H., Koustov, A. V., Shep-
 920 herd, S. G., ... Kikuchi, T. (2019). Review of the accomplishments of mid-
 921 latitude super dual auroral radar network (superdarn) hf radars. *Progress in*
 922 *Earth and Planetary Science*, *6*(1), 27. doi: 10.1186/s40645-019-0270-5
- 923 Press, W. H. and Teukolsky, S. A. and Vetterling W. T. and Flannery B. P. (2007).
 924 *Numerical recipes: The art of scientific computing.* Cambridge University
 925 Press.
- 926 Reiff, P. H., & Burch, J. (1985). Imf by-dependent plasma flow and birkeland

- 927 currents in the dayside magnetosphere: 2. a global model for northward and
 928 southward imf. *Journal of Geophysical Research: Space Physics*, 90(A2),
 929 1595–1609. doi: 10.1029/JA090iA02p01595
- 930 Ruohoniemi, J. M., & Baker, K. B. (1998). Large-scale imaging of high-latitude con-
 931 vection with Super Dual Auroral Radar Network HF radar observations. *Jour-
 932 nal of Geophysical Research*, 103(A9), 20797. doi: 10.1029/98JA01288
- 933 Ruohoniemi, J. M., & Greenwald, R. A. (1996). Statistical patterns of high-latitude
 934 convection obtained from Goose Bay HF radar observations. *Journal of Geo-
 935 physical Research*, 101(A10), 21743. Retrieved from [http://doi.wiley.com/
 936 10.1029/96JA01584](http://doi.wiley.com/10.1029/96JA01584) doi: 10.1029/96JA01584
- 937 Ruohoniemi, J. M., & Greenwald, R. A. (2005). Dependencies of high-latitude
 938 plasma convection: Consideration of interplanetary magnetic field, seasonal,
 939 and universal time factors in statistical patterns. *Journal of Geophysical Re-
 940 search: Space Physics*, 110(A09204). doi: 10.1029/2004JA010815
- 941 Russell, C. T. (1972). The configuration of the magnetosphere. In *Critical problems
 942 of magnetospheric physics* (p. 1).
- 943 Sangha, H., Milan, S. E., Carter, J. A., Fogg, A. R., Anderson, B. J., Korth, H.,
 944 & Paxton, L. J. (2020). Bifurcated region 2 field-aligned currents asso-
 945 ciated with substorms. *Journal of Geophysical Research: Space Physics*,
 946 125(1), e2019JA027041. Retrieved from [https://agupubs.onlinelibrary
 947 .wiley.com/doi/abs/10.1029/2019JA027041](https://agupubs.onlinelibrary.wiley.com/doi/abs/10.1029/2019JA027041) (e2019JA027041
 948 10.1029/2019JA027041) doi: <https://doi.org/10.1029/2019JA027041>
- 949 Shepherd, S. G., & Ruohoniemi, J. M. (2000). Electrostatic potential patterns in
 950 the high-latitude ionosphere constrained by superdarn measurements. *Journal
 951 of Geophysical Research: Space Physics*, 105(A10), 23005-23014. Retrieved
 952 from [https://agupubs.onlinelibrary.wiley.com/doi/abs/10.1029/
 953 2000JA000171](https://agupubs.onlinelibrary.wiley.com/doi/abs/10.1029/2000JA000171) doi: 10.1029/2000JA000171
- 954 Smith, R. H. (2012). Effects of ionospheric conductance on magnetosphere-
 955 ionosphere coupling. *ProQuest Dissertations and Theses*, 107. Retrieved
 956 from <http://proquest.umi.com/login/athens> (Copyright - Database
 957 copyright ProQuest LLC; ProQuest does not claim copyright in the individual
 958 underlying works; Last updated - 2022-01-05)
- 959 SuperDARN Data Analysis Working Group, P. m., Thomas, E. G., Ponomarenko,
 960 P. V., Bland, E. C., Burrell, A. G., Kotyk, K., ... Walach, M.-T. (2018,
 961 January). *Superdarn radar software toolkit (rst) 4.1*. Retrieved from
 962 <https://doi.org/10.5281/zenodo.1143675> doi: 10.5281/zenodo.1143675
- 963 Tanaka, T. (2001). Interplanetary magnetic field b y and auroral conductance ef-
 964 fects on high-latitude ionospheric convection patterns. *Journal of Geophysical
 965 Research: Space Physics*, 106(A11), 24505-24516. Retrieved from [https://
 966 agupubs.onlinelibrary.wiley.com/doi/abs/10.1029/2001JA900061](https://agupubs.onlinelibrary.wiley.com/doi/abs/10.1029/2001JA900061) doi:
 967 <https://doi.org/10.1029/2001JA900061>
- 968 Taylor, J. R., Cowley, S. W. H., Yeoman, T. K., Lester, M., Jones, T. B., Green-
 969 wald, R. A., ... Hairston, M. R. (1998). Superdarn studies of the ionospheric
 970 convection response to a northward turning of the interplanetary magnetic
 971 field. *Annales Geophysicae*, 16(5), 549–565. Retrieved from [https://doi.org/
 972 10.1007/s00585-998-0549-0](https://doi.org/10.1007/s00585-998-0549-0) doi: 10.1007/s00585-998-0549-0
- 973 Thomas, E. G., & Shepherd, S. G. (2018, apr). Statistical Patterns of Ionospheric
 974 Convection Derived From Mid-latitude, High-Latitude, and Polar Super-
 975 DARN HF Radar Observations. *Journal of Geophysical Research: Space
 976 Physics*, 123(4), 3196–3216. Retrieved from [http://doi.wiley.com/10.1002/
 977 2018JA025280](http://doi.wiley.com/10.1002/2018JA025280) doi: 10.1002/2018JA025280
- 978 Thomas, E. G., & Shepherd, S. G. (2022). Virtual height characteristics of
 979 ionospheric and ground scatter observed by mid-latitude superdarn hf
 980 radars. *Radio Science*, 57(6), e2022RS007429. Retrieved from [https://
 981 agupubs.onlinelibrary.wiley.com/doi/abs/10.1029/2022RS007429](https://agupubs.onlinelibrary.wiley.com/doi/abs/10.1029/2022RS007429)

- 982 (e2022RS007429 2022RS007429) doi: <https://doi.org/10.1029/2022RS007429>
983 Walach, M.-T. (2022, October). *[dataset]*. Lancaster University PURE. Re-
984 trieved from <https://doi.org/10.17635/lancaster/researchdata/571> doi:
985 10.17635/lancaster/researchdata/571
- 986 Walach, M.-T., & Grocott, A. (2019). Superdarn observations during geomagnetic
987 storms, geomagnetically active times, and enhanced solar wind driving. *Jour-*
988 *nal of Geophysical Research: Space Physics*, *124*(7), 5828-5847. Retrieved
989 from [https://agupubs.onlinelibrary.wiley.com/doi/abs/10.1029/](https://agupubs.onlinelibrary.wiley.com/doi/abs/10.1029/2019JA026816)
990 [2019JA026816](https://agupubs.onlinelibrary.wiley.com/doi/abs/10.1029/2019JA026816) doi: 10.1029/2019JA026816
- 991 Walach, M.-T., Grocott, A., & Milan, S. E. (2021). Average ionospheric electric field
992 morphologies during geomagnetic storm phases. *Journal of Geophysical Re-*
993 *search: Space Physics*, *126*(4), e2020JA028512. Retrieved from [https://](https://agupubs.onlinelibrary.wiley.com/doi/abs/10.1029/2020JA028512)
994 agupubs.onlinelibrary.wiley.com/doi/abs/10.1029/2020JA028512
995 (e2020JA028512 2020JA028512) doi: <https://doi.org/10.1029/2020JA028512>
- 996 Walach, M.-T., Grocott, A., Staples, F., & Thomas, E. G. (2022). Super dual au-
997 roral radar network expansion and its influence on the derived ionospheric
998 convection pattern. *Journal of Geophysical Research: Space Physics*, *127*(2),
999 e2021JA029559. doi: 10.1029/2021JA029559
- 1000 Walach, M.-T., Milan, S. E., Yeoman, T. K., Hubert, B. A., & Hairston, M. R.
1001 (2017). Testing nowcasts of the ionospheric convection from the expand-
1002 ing and contracting polar cap model. *Space Weather*, *15*(4), 623-636. doi:
1003 10.1002/2017SW001615
- 1004 Walsh, A. P., Haaland, S., Forsyth, C., Keese, A. M., Kissinger, J., Li, K., ...
1005 Taylor, M. G. G. T. (2014). Dawn-dusk asymmetries in the coupled solar
1006 wind-magnetosphere-ionosphere system: a review. *Annales Geophysicae*, *32*(7),
1007 705-737. Retrieved from [https://angeo.copernicus.org/articles/32/705/](https://angeo.copernicus.org/articles/32/705/2014/)
1008 [2014/](https://angeo.copernicus.org/articles/32/705/2014/) doi: 10.5194/angeo-32-705-2014
- 1009 Yeh, H.-C., Foster, J., Rich, F. J., & Swider, W. (1991). Storm time elec-
1010 tric field penetration observed at mid-latitude. *Journal of Geophysical*
1011 *Research: Space Physics*, *96*(A4), 5707-5721. Retrieved from [https://](https://agupubs.onlinelibrary.wiley.com/doi/abs/10.1029/90JA02751)
1012 agupubs.onlinelibrary.wiley.com/doi/abs/10.1029/90JA02751 doi:
1013 <https://doi.org/10.1029/90JA02751>